Journal of Wind Engineering & Industrial Aerodynamics 233 (2023) 105284

Contents lists available at ScienceDirect

Journal of Wind Engineering & Industrial Aerodynamics

journal homepage: www.elsevier.com/locate/jweia

Systematic investigation of effect of rotor solidity on vertical-axis wind turbines: Power performance and aerodynamics analysis

Limin Kuang [a], Rui Zhang [a], Jie Su [a], Yixiao Shao [a], Kai Zhang [a,b,c], Yaoran Chen [a], Zhihao Zhang [a], Yu Tu [a], Dai Zhou [a,b,c,*], Zhaolong Han [a,b,c], Yan Bao [a,b,c], Yong Cao [a,b,c]

[a] School of Naval Architecture, Ocean and Civil Engineering, Shanghai Jiao Tong University, Shanghai, 200240, China
[b] State Key Laboratory of Ocean Engineering, Shanghai Jiao Tong University, Shanghai, 200240, China
[c] Shanghai Key Laboratory for Digital Maintenance of Buildings and Infrastructure, Shanghai Jiao Tong University, Shanghai, 200240, China

ARTICLE INFO

Keywords:
Urban VAWT
Rotor solidity
Power performance
Aerodynamics
Reynolds number effect

ABSTRACT

Small-scale vertical-axis wind turbines (VAWTs) are receiving growing interest for applications in urban areas. However, the unsatisfactory power performance, mainly induced by the complex blade aerodynamics, restricts their development. Optimizing the turbine geometry is expected to improve the blade aerodynamics. In the present study, the effect of rotor solidity on the power performance and aerodynamics of VAWTs is systematically investigated using high-fidelity improved delayed detached-eddy simulations. A wide range of rotor solidity from 0.12 to 0.6 is studied for VAWTs with different numbers of blades, i.e., two- and three-bladed VAWTs. Also, different rotor diameters (0.5 m–2 m), covering VAWTs from domestic to building integration, are compared to explore the scale effect. In addition, the Reynolds number effect induced by the change of turbine geometry is considered and its impact on the solidity effect is elucidated. The results show that a low to moderate rotor solidity (e.g., lower than 0.3) allows the VAWT to achieve appreciable peak power performance. When the inflow velocity is fixed, for a given relatively low rotor solidity (e.g., 0.12), the two-bladed design is expected to achieve higher peak turbine power, while the three-bladed design is more advantageous when the rotor solidity is relatively high (e.g., 0.36). For a given rotor solidity, VAWTs with smaller rotor diameters perform relatively better due to the diminished tip loss effect. The effects of number of blades and rotor diameter are strongly affected by the variation of the chord-based Reynolds number. This study would support the optimal design of urban VAWTs.

1. Introduction

With the increasing consumption of fossil fuels, the exploitation of renewable energy is becoming an essential issue for the sustainability of human society (Celik et al., 2020). Over the past decade, renewable energy has experienced significant growth in new power generation worldwide, with wind energy accounting for a large portion of that growth (Al-Shetwi, 2022). As one of the key wind energy conversion devices, wind turbines have been continuously developed. The rotation axis direction divides wind turbines into two categories, i.e., vertical-axis wind turbines (VAWTs) and horizontal-axis wind turbines (HAWTs) (Dilimulati et al., 2018), (Yan et al., 2021). With high efficiency and clear aerodynamics in steady winds, HAWTs have long suppressed VAWTs and dominated the global commercial market (Elkhoury et al., 2015). However, in recent years, there has been a growing interest for applying small-scale VAWTs in urban areas (Posa, 2021). This could be attributed to the unique advantages of VAWTs, i.e., omnidirectionality, less noise pollution, and visual friendliness (Hand et al., 2021), (Rezaeiha et al., 2018a).

Nevertheless, the unsatisfactory power performance restricts the large-scale applications of VAWTs, in which the complex blade aerodynamics plays a crucial role (Kuang et al., 2022a). The frequently occurring undesired flow phenomena, such as flow separation, dynamic stall, and blade-vortex interaction, significantly alter the flow patterns on the blades and degrade their power generation capacity (Rezaeiha, 2019). Therefore, it is important to explore the blade aerodynamics for improving the power performance of VAWTs.

The blade aerodynamics is fundamentally determined by the operational and geometrical properties of the wind turbine. It is therefore imperative to understand the effects of the corresponding parameters on

* Corresponding author. School of Naval Architecture, Ocean and Civil Engineering, Shanghai Jiao Tong University, Shanghai, 200240, China.
E-mail address: zhoudai@sjtu.edu.cn (D. Zhou).

https://doi.org/10.1016/j.jweia.2022.105284
Received 16 August 2022; Received in revised form 17 December 2022; Accepted 17 December 2022
Available online 11 January 2023

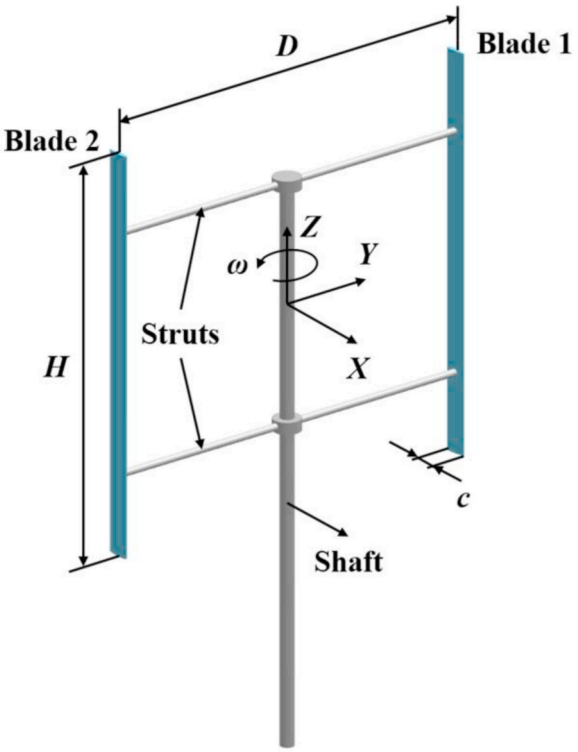

Fig. 1. Schematic of the reference VAWT.

VAWTs. Extensive studies have been conducted to investigate the effects of operational parameters such as tip speed ratio (TSR) (Rezaeiha et al., 2018a), (Posa, 2020), turbulence intensity (Molina et al., 2019), (Bhargav et al., 2016), and Reynolds number (Zanforlin and Deluca, 2018), (Li et al., 2022). These studies revealed the turbine aerodynamics under different operating conditions and can support the performance improvement of VAWTs. The investigation of geometrical parameters has also reached a fairly comprehensive level, in which the effects of airfoil shape (Zhang et al., 2020), (Tirandaz and Rezaeiha, 2021), blade pitch angle (Rezaeiha et al., 2017a), (Chen et al., 2019), shaft diameter (Rezaeiha et al., 2017b), rotor solidity (Rezaeiha et al., 2018b), (Lam et al., 2018), and blade aspect ratio (Li et al., 2017), (Peng et al., 2019) were studied experimentally and numerically. Note that in numerical studies, the computational fluid dynamics (CFD) method is extensively employed due to its high fidelity and capability to obtain key flow information around the blades (Su et al., 2020).

The rotor solidity reflects the relationship between the projected area of the blades and the swept area of the wind turbine, which for VAWTs is calculated as $\sigma = nc/D$, in which c, n, and D are the chord length, number of blades, and rotor diameter, respectively (Rezaeiha et al., 2018b). As it combines various geometrical parameters, the rotor solidity is expected to have a significant impact on wind turbines and therefore attracts the attention of researchers. Hassan et al. (2016) employed the CFD method to investigate the effect of rotor solidity on the power performance of VAWTs. The results showed that the maximum power coefficient and optimal TSR (TSR_{opt}) of the VAWT decreased with the increase of the rotor solidity. Gosselin et al. (2016) numerically explored the effect of rotor solidity on the aerodynamic performance of VAWTs. They found that the best performing VAWT had a rotor solidity of about 0.2. Also, less torque ripples were observed as the number of blades increased, which was further confirmed by Zhu et al. (2019). Subramanian et al. (2017) studied the effect of rotor solidity on the power performance of VAWTs using the transition shear stress transport (SST) turbulence model. They observed that two-bladed VAWTs performed better than three-bladed ones (with the same chord length) at high TSRs. This was due to the increased incidence of blade-vortex interactions for higher rotor solidities. Rezaeiha et al. (2018b) analyzed the effect of rotor solidity on the aerodynamic performance of VAWTs using the Reynolds-Averaged Navier-Stokes (RANS) method. It was concluded that the relatively low rotor solidity is more suitable for urban VAWTs that are frequently operated at moderate to high TSRs. In addition, the TSR_{opt} was found to depend only on the rotor solidity. The experimental studies conducted by Lam et al. (2018), Eboibi et al. (2016), and Li et al. (2016) verified the corresponding effects and provided valuable suggestions for selecting the rotor solidity.

The above studies elucidated the effect of rotor solidity and established a solid foundation for the optimal design of VAWTs. However, there are still some limitations that need further investigation: (1) Most numerical studies are based on two-dimensional CFD simulations. The inherent drawbacks of two-dimensional modeling (e.g., assuming an infinite blade span and neglecting the tip loss effect) will lead to an overestimation of turbine performance (McIntosh, 2009), (Hand and Cashman, 2017), especially for high-solidity VAWTs (long chord length leads to small blade aspect ratio), thus affecting the simulation reliability. Also, the unavailability of the spanwise flow patterns on the blades restricts the insight into the aerodynamic mechanisms. (2) Most studies focused on modifying the chord length and number of blades, while the effect of rotor diameter was rarely considered. Urban VAWTs cover a wide range from domestic to building integration, in which the scale effect is worth investigating. Understanding the performance of VAWTs with different rotor diameters can help select the turbine size. (3) The effect of rotor solidity may be affected by the Reynolds number effect induced by the change of turbine geometry (Rezaeiha et al., 2018b). However, this potential impact has rarely been investigated. Eboibi et al. (2016) experimentally compared the aerodynamic performance of VAWTs with different chord lengths at variable and fixed Reynolds numbers. The results showed that the solidity effect would present different characteristics when the Reynolds number was changed. Rezaeiha et al. (2018b) numerically compared the aerodynamic performance of VAWTs with different number of blades at fixed Reynolds numbers and obtained valuable results, however, limited comparisons were made with the cases of variable Reynolds numbers. Therefore, the knowledge of how the Reynolds number affects the solidity effect is still not very clear, especially when modifying the number of blades and the rotor diameter.

Therefore, in the present study: (1) Using high-fidelity three-dimensional CFD simulations, the effect of rotor solidity is investigated over a wide range from a low value of 0.12 to a high value of 0.6 for VAWTs with different numbers of blades, i.e., two- and three-bladed VAWTs. (2) In addition to the turbine performance (i.e., power coefficient), the dynamic loads and flow patterns on the blades are systematically analyzed to reveal the aerodynamic mechanisms. (3) Extensive simulations are performed for VAWTs with different rotor diameters and a fixed moderate rotor solidity of 0.24. This adds new knowledge to the scale effect. The rotor diameter ranges from 0.5 m to 2 m, covering VAWTs from domestic to building integration. (4) The Reynolds number effect induced by the change of turbine geometry is considered. Comparative analyses are conducted at variable and fixed chord-based Reynolds numbers to better elucidate the solidity effect.

Based on high-fidelity CFD simulations, the present study aims to provide an in-depth understanding of the effect of rotor solidity on the power performance and aerodynamics of VAWTs so as to support their optimal design. The main contributions can be summarized in two aspects: (1) The effects of chord length, number of blades, and rotor diameter are systematically investigated, accompanied by an exploration of aerodynamic mechanisms, e.g., dynamic stall and tip loss effect. This helps to select the solidity and size of urban VAWTs. (2) The turbine aerodynamics at variable and fixed chord-based Reynolds numbers are thoroughly compared, which enriches the knowledge of how the Reynolds number effect affects the solidity effect.

The remainder of the present study is organized as follows: Section 2

Table 1
Test cases for investigating the effect of rotor solidity: (a) variable Re_c part; (b) fixed Re_c part.

(a)	Variable Re_c							
Parameter	n	σ	C (m)	D (m)	TSR_{opt}	U_0 (m/s)	ω (rad/s)	Re_c ($\times 10^5$)
c	2	0.12	0.06	1	3.805	9.3	70.773	1.71
		0.18	0.09		3.129		58.199	2.21
		0.24	0.12		2.702		50.257	2.64
		0.30	0.15		2.397		44.584	3.02
		0.36	0.18		2.164		40.250	3.38
	3	0.12	0.04	1	3.805	9.3	70.773	1.14
		0.24	0.08		2.702		50.257	1.76
		0.36	0.12		2.164		40.250	2.25
		0.48	0.16		1.824		33.926	2.68
		0.60	0.20		1.581		29.407	3.06
n	2	0.12	0.06	1	3.805	9.3	70.773	1.71
	3		0.04					1.14
	2	0.24	0.12	1	2.702	9.3	50.257	2.64
	3		0.08					1.76
	2	0.36	0.18	1	2.164	9.3	40.250	3.38
	3		0.12					2.25
D	2	0.24	0.06	0.5	2.702	9.3	100.514	1.32
			0.09	0.75			67.010	1.98
			0.12	1			50.257	2.64
			0.15	1.25			40.206	3.30
			0.18	1.5			33.505	3.96
			0.21	1.75			28.718	4.62
			0.24	2			25.129	5.27
(b)	Fixed Re_c							
Parameter	n	σ	C (m)	D (m)	TSR_{opt}	U_0 (m/s)	ω (rad/s)	Re_c ($\times 10^5$)
n	2	0.12	0.06	1	3.805	9.3	70.773	1.71
	3		0.04			13.95	106.160	
	2	0.24	0.12	1	2.702	9.3	50.257	2.64
	3		0.08			13.95	75.386	
	2	0.36	0.18	1	2.164	9.3	40.250	3.38
	3		0.12			13.95	60.376	
D	2	0.24	0.06	0.5	2.702	18.6	201.029	2.64
			0.12	1		9.3	50.257	
			0.15	1.25		7.44	32.165	
			0.24	2		4.65	12.564	

describes the geometrical properties of the reference VAWT and details the test cases. Section 3 provides the information of the numerical model. The results and discussion of the effect of rotor solidity are presented in Section 4 and 5. Section 6 summarizes the conclusions.

2. Geometric model

2.1. Reference turbine

A small-scale H-type VAWT designed by Tescione et al. (2014) is selected as the reference turbine for the present study. This VAWT has been extensively selected as a benchmark for validation and optimization in previous studies due to its proper size and appreciable power performance (Mendoza et al., 2019), (Rezaeiha et al., 2019). Fig. 1 presents a schematic of the selected VAWT. The VAWT rotates counterclockwise at a prescribed angular velocity ω. The chord length c, rotor diameter D, span length H, and rotor solidity σ of the VAWT are 0.06 m, 1 m, 1 m, and 0.12, respectively. The blade section has a NACA0018 profile, which has relatively good aerodynamic performance among symmetric NACA airfoils and is extensively employed in the design of VAWTs (Claessens, 2006), (Rogowski et al., 2020). Note that the shaft and struts are neglected in the numerical modeling because of their small impact on the turbine aerodynamics (Lei et al., 2017).

2.2. Test cases

The present study attempts to investigate the effect of rotor solidity on the power performance and aerodynamics of VAWTs. Three key geometrical parameters, i.e., chord length, number of blades, and rotor diameter, are studied over a wide and reasonable range. The Reynolds number effect induced by the change of turbine geometry is also considered.

Table 1 lists the test cases set up for the present study. The test cases are classified into two parts, bounded by whether the chord-based Reynolds number Re_c is variable or fixed. The modification of each parameter is based on the reference VAWT case. For the variable Re_c part, the inflow velocity U_0 is fixed at 9.3 m/s and the rotor solidity is changed via the chord length. The value of σ varies in the range of

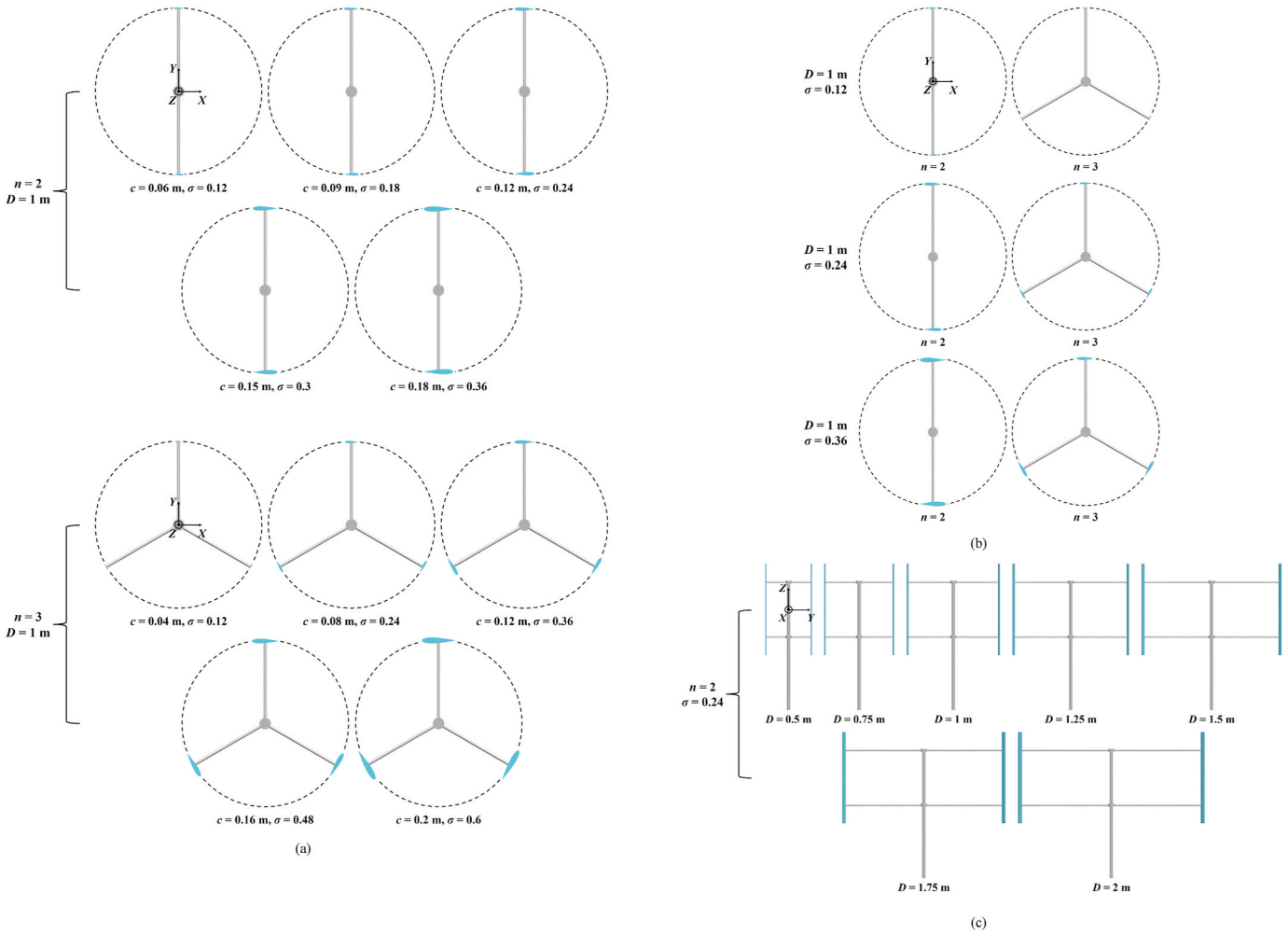

Fig. 2. Schematic of the test cases: (a) modification of chord length; (b) modification of number of blades; (c) modification of rotor diameter.

0.12–0.36 and 0.12–0.6 for $n = 2$ and 3, respectively (refer to Fig. 2(a)), which covers the typical rotor solidities employed in the design of VAWTs. Also, the effect of number of blades is investigated by comparing the performance of VAWTs with different numbers of blades and the same rotor solidity (refer to Fig. 2(b)). The rotor solidities of 0.12, 0.24 and 0.36 are selected considering the turbine performance and the generalizability of the present study. In addition, extensive simulations are performed for VAWTs with different rotor diameters and a fixed rotor solidity of 0.24 to explore the scale effect (refer to Fig. 2(c)). For the fixed Re_c part, when the turbine geometry changes, the inflow velocity is modified correspondingly to keep the Re_c invariant. For example, the inflow velocity is modified to 13.95 m/s for all three-bladed VAWT cases to reach the Re_c for the two-bladed VAWT cases. Note that only the TSR_{opt} is considered in both parts, as it represents one of the most typical operating conditions for wind turbines. The TSR_{opt} of the VAWT is calculated using the TSR_{opt}-rotor solidity correlation proposed by Rezaeiha et al. (2018b), which is expressed as:

$$TSR_{opt} = 2.693\sigma^{-0.329} - 1.605 \quad (1)$$

3. Numerical model

In the present study, the commercial CFD software STAR-CCM+ 13.04 (CD-adapco, 2018) is utilized to perform the transient simulations. The SST k-ω improved delayed detached-eddy simulation (IDDES) is employed to handle the turbulence modeling issues. On the one hand, the IDDES retains the advantages of DES and DDES, e.g., more accurate than the RANS method and less costly than the large-eddy simulation (LES) (Lei et al., 2017). On the other hand, the IDDES resolves the issue of log-layer mismatch in DES and DDES by introducing several functions of wall-modeled LES (Shur et al., 2008). These characteristics make the IDDES a promising hybrid RANS/LES approach for simulating complex turbulent flows. Note that the SST k-ω IDDES has been shown to be superior in simulating the turbine aerodynamics in the authors' previous studies (Kuang et al., 2022a), (Kuang et al., 2021).

3.1. Computational domain

Fig. 3 presents a schematic of the computational domain for the reference VAWT case. The domain is composed of a fixed region and a rotational region. The exchange of physical information between the two regions is achieved by the sliding mesh technique. Based on the studies of Su et al. (2020) and Kuang et al. (2021), (Kuang et al., 2022b), the height, length, and width of the fixed region are set to 5H, 25D, and 10D, respectively. The height and diameter of the rotational region are set to 1.5H and 1.5D, respectively.

For the boundary conditions, a uniform inflow of 9.3 m/s and a gauge pressure of 0.0 Pa are specified at the inlet and outlet of the computational domain, respectively. The inlet turbulence intensity is set to 0.5%. Note that the turbulence intensity is taken to fit the low turbulence environment of the experiments (Tescione et al., 2014). The four sides of the domain are set as symmetry planes and a no-slip wall

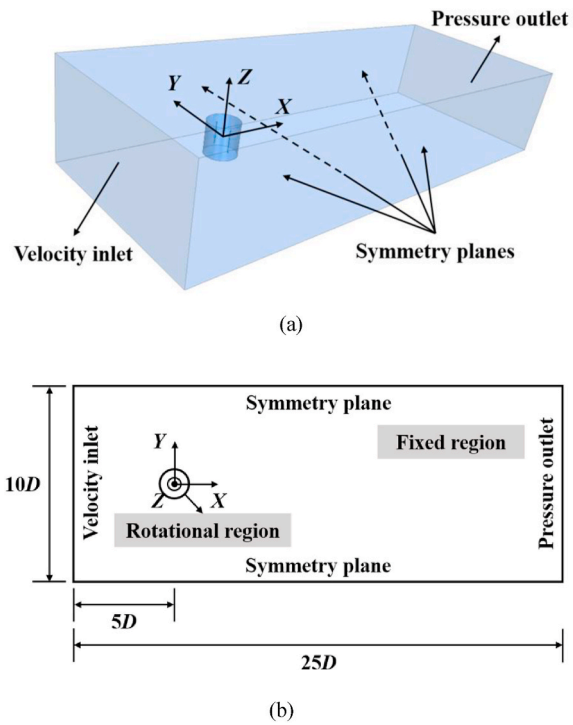

Fig. 3. Schematic of the computational domain for the reference VAWT case: (a) three-dimensional view; (b) plan view.

boundary is assigned to the turbine surface.

3.2. Mesh topology

Fig. 4 presents a schematic of the mesh topology for the reference VAWT case. Refined hexahedral grids are distributed around the turbine and in the wake region. High-resolution boundary layer grids are generated in the vicinity of the blades to capture the behavior of the viscous sublayer flow. To fulfill the simulation demand of $y^+ < 1$ for the SST k-ω IDDES (Lei et al., 2017), the total thickness, growth rate, and layer number of the boundary layer grids are set to 0.0033 m, 1.2, and 27, respectively. The number of grids for the reference VAWT case is about 7.7 million. Note that the validity of the mesh topology has been thoroughly checked in STAR-CCM+. The mesh independence test for the reference VAWT case is provided in Supplementary material S.1.

3.3. Solver settings

Table 2 lists the solver settings employed in the present study. The selection of these settings is based on the authors' previous studies (Kuang et al., 2022a), (Kuang et al., 2022b) and also refers to the CFD guidelines for VAWTs proposed by Rezaeiha et al. (2017c) and the guidelines for transient simulations in the STAR-CCM + User Guide (CD-adapco, 2018). The solution validation of the numerical model is provided in Supplementary material S.2. Note that the aerodynamic parameters of the VAWT are sampled if the changes in the average values between two consecutive turbine revolutions are less than 0.1% (Balduzzi et al., 2016).

Table 2
Solver settings.

Flow solver		Segregated
Discretization scheme	Time	Second-order
	Convection	Hybrid second-order upwind/bounded central-differencing
Pressure-velocity coupling algorithm		SIMPLE
Physical time step		$T/360$ (T denotes the period of one turbine revolution)
Maximum inner iteration		20

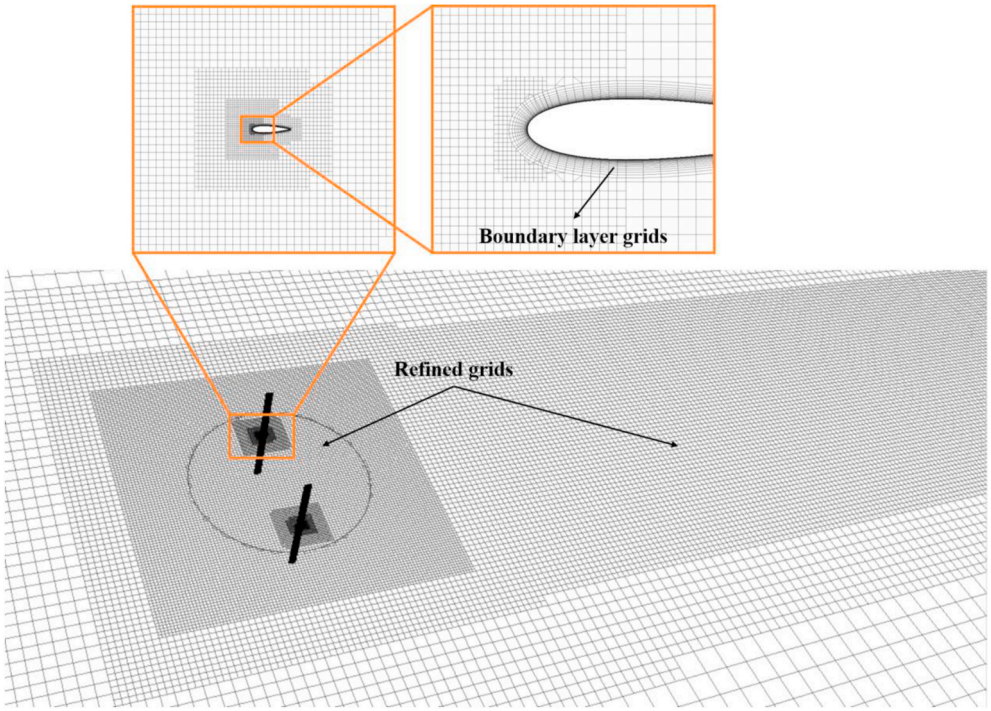

Fig. 4. Schematic of the mesh topology for the reference VAWT case.

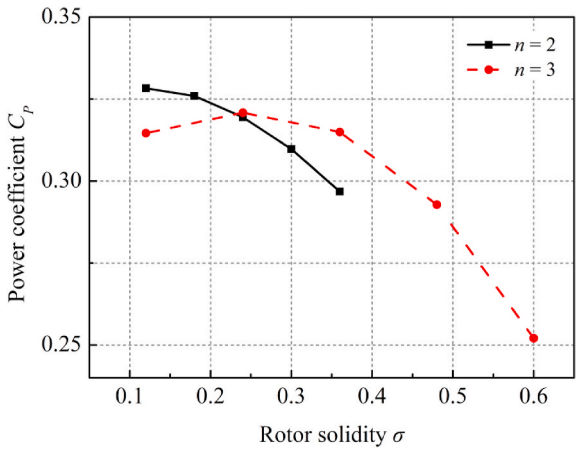

Fig. 5. Average power coefficients of two- and three-bladed VAWTs with different rotor solidities. (Modifying chord length, $D = 1$ m).

4. Effect of rotor solidity at variable chord-based Reynolds numbers

In this section, the effect of rotor solidity on the power performance and aerodynamics of VAWTs at variable chord-based Reynolds numbers is investigated. As listed in Table 1(a), the chord length, number of blades, and rotor diameter are modified to change the turbine geometry, while the inflow velocity is fixed. The turbine performance as well as the dynamic loads and flow patterns on the blades are systematically analyzed.

4.1. Effect of chord length

Fig. 5 shows the average power coefficients C_P of two- and three-bladed VAWTs with different rotor solidities. The rotor solidity is changed by modifying the chord length (refer to Table 1(a) and Fig. 2 (a)). It can be seen that for the three-bladed VAWT, the value of C_P first increases and then decreases as σ increases from 0.12 to 0.6, with the optimal C_P occurring at $\sigma = 0.24$. However, the value of C_P is found to decrease monotonically with the increase of σ for the two-bladed VAWT. The absence of the inflection point indicates that the optimal C_P for the two-bladed VAWT occurs at $\sigma \leq 0.12$, which implies a shorter chord length. This inconsistency may be due to the Reynolds number effect induced by the different chord lengths, in which the chord length of the two-bladed VAWT is 1.5 times longer than that of the three-bladed one for the same σ, implying that the two-bladed VAWT experiences a higher Re_c. Overall, in terms of modifying the chord length, a low to moderate rotor solidity allows the VAWT to achieve appreciable peak power performance, while an excessively high rotor solidity will reduce the peak turbine power.

Fig. 6 shows the instantaneous angles of attack α, lift coefficients C_L, and drag coefficients C_D of the blades during one turbine revolution for different rotor solidities. Note that to simplify the performance analysis of VAWTs, the turbine induction is neglected in the present study and thus the geometrical angle of attack is employed. Since the TSR_{opt} decreases with the increase of σ (refer to Eq. (1)), the oscillation amplitude of α gradually increases as σ increases from 0.12 to 0.6 and is expected to exceed the static stall angle of NACA0018 airfoil at certain azimuthal angles θ. For the curves of C_L, sinusoidal oscillations are observed in the upwind region ($0^\circ \leq \theta \leq 180^\circ$), which are similar to those of α. Also, the peak value of C_L increases with the increase of σ, and the decay time from peak to valley is shortened. In the case of the three-bladed VAWT, for example, the oscillation amplitude of C_L in the upwind region for $\sigma = 0.6$ is 135.23% higher than that for $\sigma = 0.12$, and the decay time is shortened by 34.43%. In the downwind region ($180^\circ \leq \theta \leq 360^\circ$), the curves of C_L do not show a sinusoidal trend and become nearly flat when $\theta \geq 240^\circ$. This can be interpreted by the fact that the rotor thrust has a significant deceleration effect on the flow field and the velocity in this region is slowed down (Rezaeiha et al., 2018a). Also, this phenomenon is found to be more intense with the increase of σ. This is because the enlarged blade surface area increases the rotor thrust. In addition, a clear inflection point is observed in the early downwind region when $\sigma \geq 0.36$. The corresponding absolute valley value increases significantly with further increase of σ, e.g., for the three-bladed VAWT, the absolute valley value of C_L is increased by 143.41% when σ is increased from 0.36 to 0.6. As a comparison, the relative increase in the absolute valley value of C_L is only 52.50% when σ increases from 0.12 to 0.36, indicating that C_L is less sensitive to the variation of σ when σ is relatively low. For the curves of C_D, a large jump is observed in the upwind region when $\sigma \geq 0.48$, which signals the occurrence of dynamic stall on the blades. Also, the intense fluctuations of C_D in the early downwind region reflect the strong blade-wake interactions, which correspond to the clear inflection points in the curves of C_L. These undesired flow phenomena lead to the deterioration of the peak power performance of VAWTs with high rotor solidities.

Fig. 7 shows the instantaneous tangential force coefficients C_T and normal force coefficients C_N of the blades during one turbine revolution for different rotor solidities. For the curves of C_T, it can be seen that the oscillation amplitude increases with the increase of σ in both upwind and downwind regions. The increased tangential load in the upwind region is the result of the larger α and higher C_L shown in Fig. 6. In the late downwind region, the effect of σ on the tangential load is negligible due to the low flow velocity. It is further observed that when σ is relatively low, the curve of C_T shows two positive peaks, in which the peak in the downwind region is lower than that in the upwind region. However, when σ increases from 0.36 to 0.6, the curve of C_T experiences a sudden drop in the late upwind region with a negative valley. Also, the peak value of C_T in the downwind region increases significantly and becomes higher than that in the upwind region. As described above, this is the result of enhanced blade-wake interactions. For the curves of C_N, a similar trend to the curves of C_L is observed, in which the higher σ increases the oscillation amplitude in the upwind region and makes the inflection point in the early downwind region more pronounced.

Fig. 8 shows the instantaneous power coefficients of the blades during one turbine revolution for different rotor solidities. It can be seen that for the two-bladed VAWT, the higher σ increases the values of C_P in nearly the entire upwind region, especially in the region of $80^\circ \leq \theta \leq 110^\circ$. For example, the peak value of C_P is increased by 9.70% when σ is increased from 0.12 to 0.24. However, these improvements diminish with further increase of σ, in which the peak value of C_P for $\sigma = 0.36$ is slightly lower than that for $\sigma = 0.3$. In the downwind region, when $\theta \geq 210^\circ$, the values of C_P are found to decrease significantly for higher σ, which leads to the decrease of the average C_P shown in Fig. 5. For the three-bladed VAWT, the peak value of C_P in the upwind region is found to decrease by 6.05% when σ is increased from 0.36 to 0.6, and the decay time of C_P is significantly shortened, which corresponds to the sudden drop of C_T associated with dynamic stall. Also, fluctuations induced by the blade-wake interactions are observed in the downwind region.

Fig. 9 shows the normalized cumulative sums of the instantaneous torque coefficients C_Q of the blades during one turbine revolution for different rotor solidities. The relative contributions of upwind and downwind regions to the turbine power are presented. It can be seen that most of the turbine power is generated in the upwind region and the higher σ promotes this trend, e.g., for the three-bladed VAWT, the relative power contribution in the upwind region is increased by 25.25% when σ is increased from 0.12 to 0.6. Since most of the energy contained in the inflow is absorbed in the upwind region, the blades in the downwind region cannot obtain sufficient driving force, thus generating a negative torque, which corresponds to the negative C_P shown in Fig. 8. To achieve appreciable peak power performance, this phenomenon should be avoided so that the turbine power cumulation maintains an

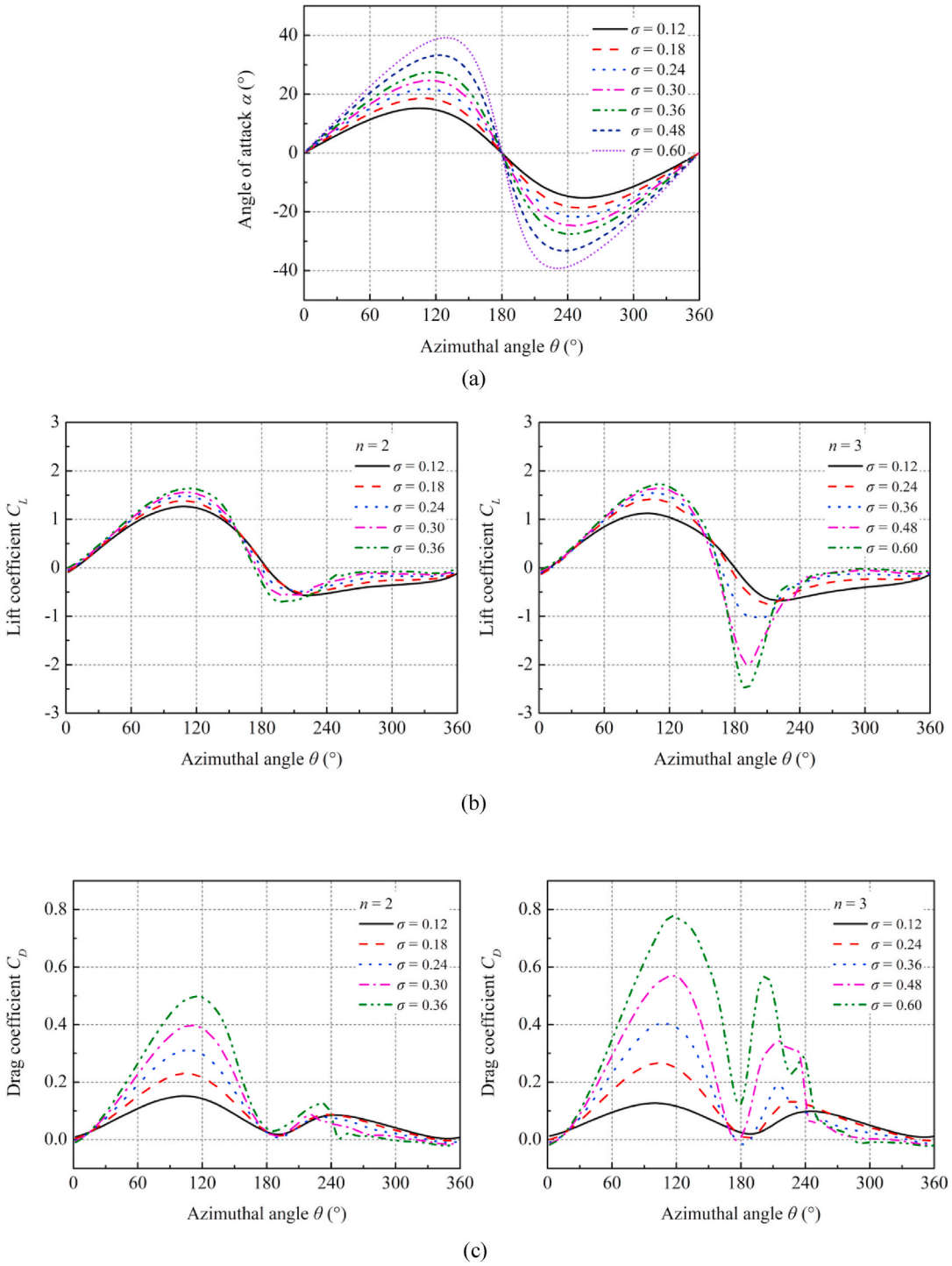

Fig. 6. Instantaneous angles of attack, lift coefficients, and drag coefficients of the blades during one turbine revolution for different rotor solidities: (a) angle of attack; (b) lift coefficient; (c) drag coefficient. (Modifying chord length, $D = 1$ m).

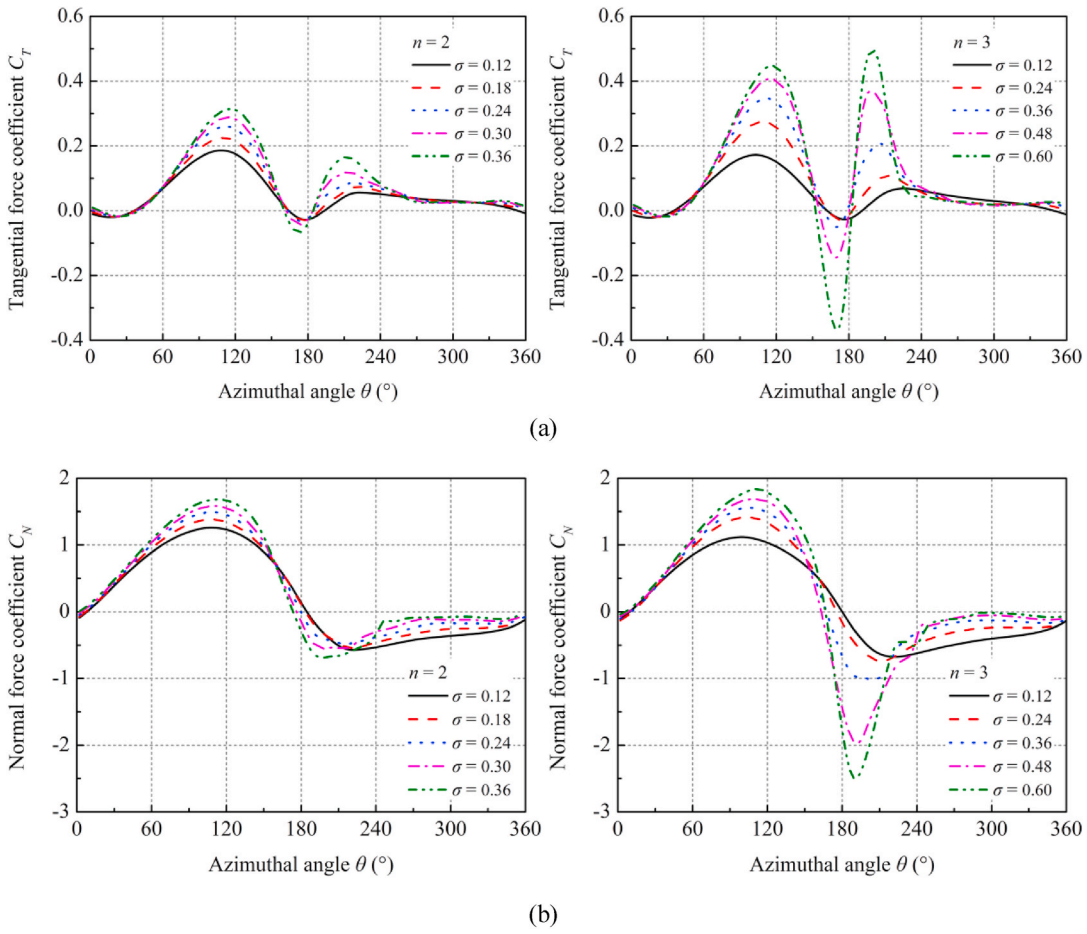

Fig. 7. Instantaneous tangential force coefficients and normal force coefficients of the blades during one turbine revolution for different rotor solidities: (a) tangential force coefficient; (b) normal force coefficient. (Modifying chord length, $D = 1$ m).

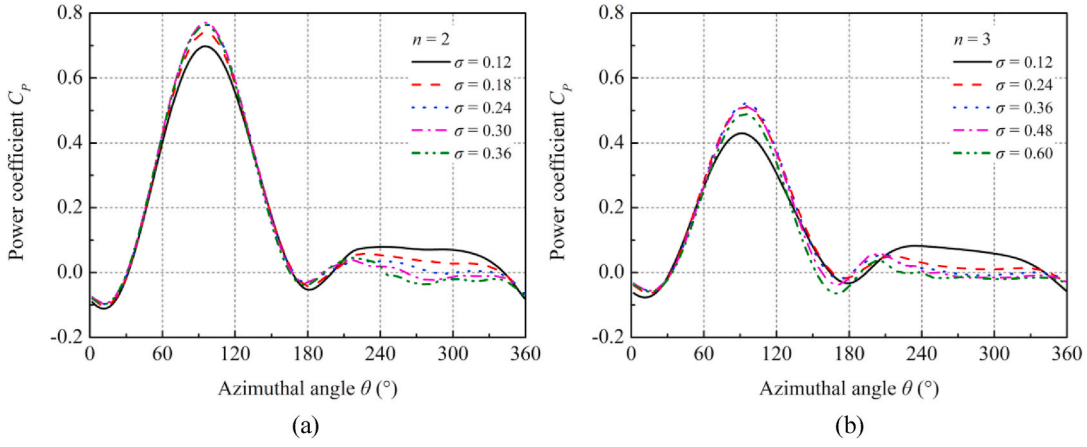

Fig. 8. Instantaneous power coefficients of the blades during one turbine revolution for different rotor solidities: (a) two-bladed VAWT; (b) three-bladed VAWT. (Modifying chord length, $D = 1$ m).

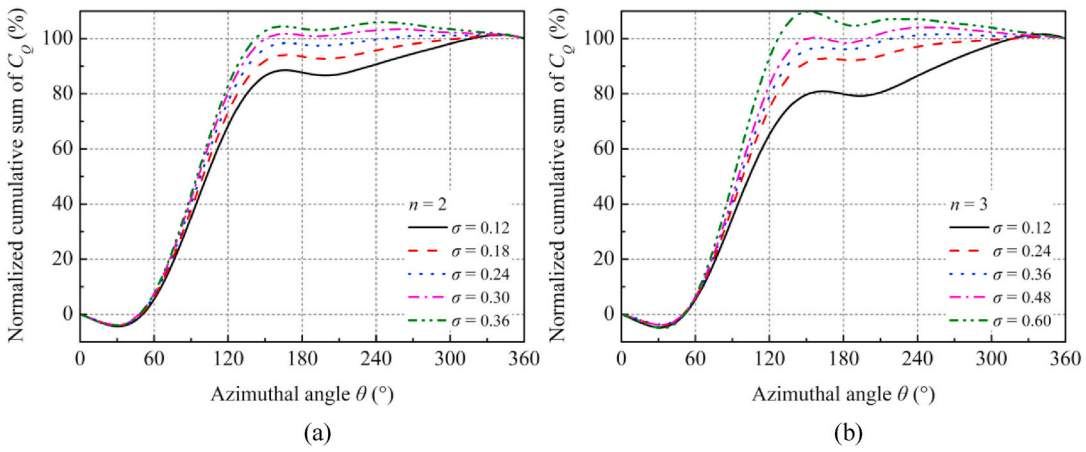

Fig. 9. Normalized cumulative sums of the instantaneous torque coefficients of the blades during one turbine revolution for different rotor solidities: (a) two-bladed VAWT; (b) three-bladed VAWT. (Modifying chord length, $D = 1$ m).

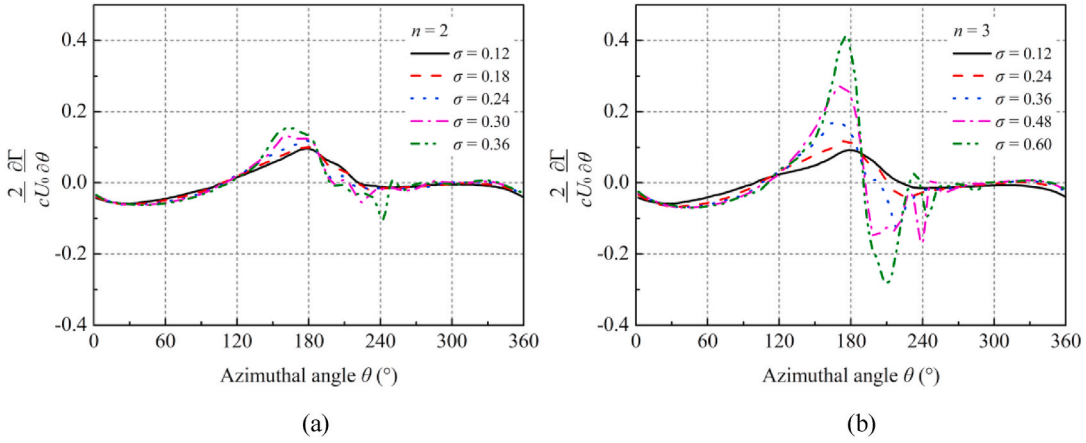

Fig. 10. Instantaneous shed vorticity strength of the blades during one turbine revolution for different rotor solidities: (a) two-bladed VAWT; (b) three-bladed VAWT. (Modifying chord length, $D = 1$ m).

upward trend. In addition, a clear curve drop is observed around $\theta = 180°$ due to the significant variations of C_L and C_D shown in Fig. 6.

Fig. 10 shows the instantaneous shed vorticity strength of the blades during one turbine revolution for different rotor solidities. The shed vorticity strength of a single blade is specified as the gradient of circulation per azimuthal angle, which is calculated as (Rezaeiha et al., 2018a), (Ferreira and Geurts, 2015):

$$\frac{\partial \Gamma}{\partial \theta} = -\frac{1}{2} U_0 c \frac{\partial C_L}{\partial \theta} \tag{2}$$

The dimensionless form of Eq. (2) is expressed as:

$$\frac{2}{U_0 c}\frac{\partial \Gamma}{\partial \theta} = -\frac{\partial C_L}{\partial \theta} \tag{3}$$

Note that the positive value of Eq. (3) indicates a counterclockwise circulation. It can be seen that in the upwind region, the shed vorticity strength gradually increases from negative to positive values. During the upstroke motion, clockwise vortices are shed from the blades as C_L increases. In contrast, counterclockwise vortices are shed during the downstroke motion, accompanied by the decrease of C_L. Compared with that in the upwind region, the shed vorticity strength in the downwind region is lower due to the flatness of the curves of C_L. Also, the higher σ is found to enhance the shed vorticity strength and bring more fluctuations in the region of $150° \leq \theta \leq 240°$, which corresponds to the large slope of the curves of C_L, indicating stronger flow separation and blade-wake interactions.

Fig. 11 illustrates the instantaneous dimensionless vorticity distributions at the mid-span section of the blades ($Z = 0$, refer to Fig. 1) for different rotor solidities. It can be seen that the increase of σ significantly changes the vorticity field around the blades. When $\sigma = 0.12$, the counterclockwise vortices are nearly attached to the suction side of the blades and the flow separation occurs at the trailing edge. As σ increases from 0.12 to 0.36, the location of flow separation shifts toward the leading edge and the roll-up vortices form near the trailing edge. Also, the strength of the vortices shedding from the blunt trailing edge is enhanced. The vorticity distributions at the tip section of the blades ($Z = 0.5H$, refer to Fig. 1) appear very different compared to those at the mid-span section, in which the flows are shown to be detached and present three-dimensional characteristics (refer to Fig. 12). This phenomenon is in agreement with the findings of Edwards (2012). Meanwhile, the increase of σ intensifies the tip loss effect, in which the clockwise tip vortices develops significantly. These flow phenomena are further confirmed by the streamline distributions on the suction side of the blades illustrated in Fig. 13. The higher σ is found to drive the bifurcation line toward the leading edge, and more complex flow patterns, such as increased number of saddle points, are observed in the spanwise direction due to the propagation of tip vortices. The change of the flow structures around the blades is mainly due to the larger α and smaller

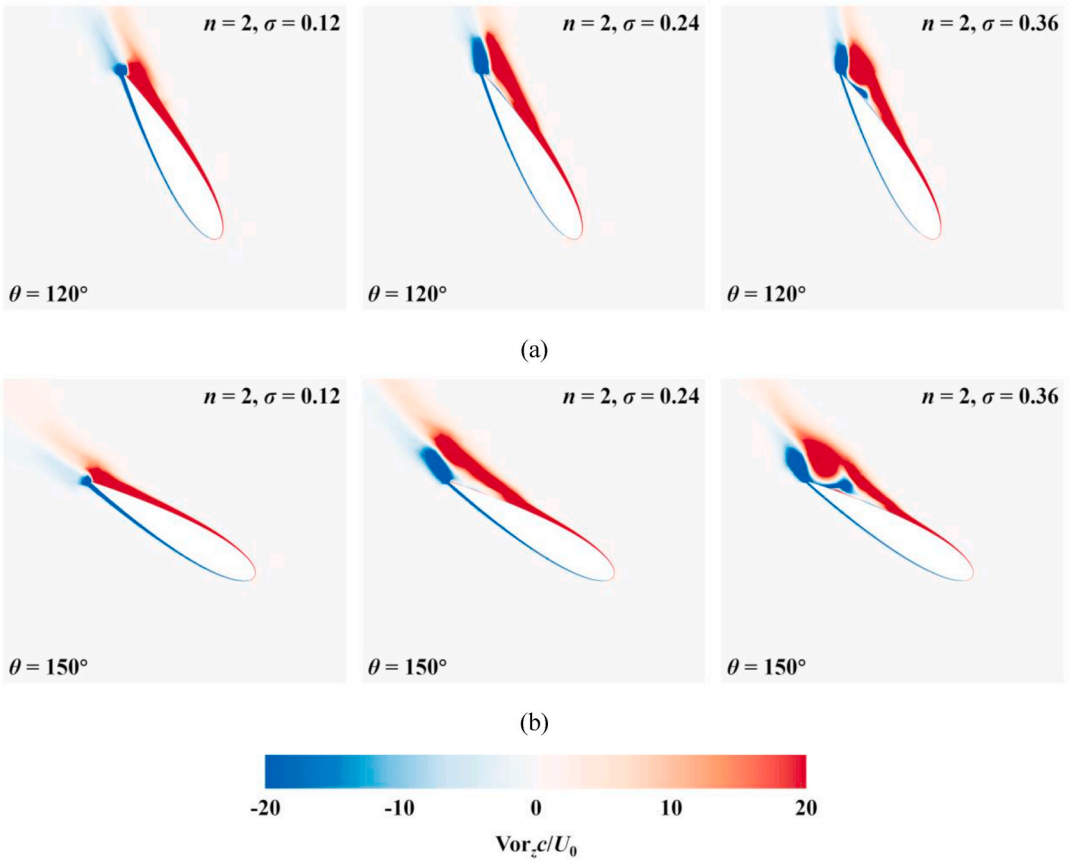

Fig. 11. Instantaneous dimensionless vorticity distributions at the mid-span section of the blades for different rotor solidities: (a) $\theta = 120°$; (b) $\theta = 150°$. (Modifying chord length, $n = 2$, $D = 1$ m).

blade aspect ratio for higher σ, which deteriorates the blade aerodynamics and leads to the decrease of C_P shown in Fig. 5. In addition, tip vortices are found to drive the bifurcation line near the blade tips toward the trailing edge and delay flow separation, which is also reported in the study of Edwards (2012).

4.2. Effect of number of blades

Fig. 14 shows the average power coefficients of VAWTs with different numbers of blades. The two- and three-bladed VAWTs have the same σ and TSR_{opt} (refer to Table 1(a) and Fig. 2(b)). It can be seen that the peak power performance of the VAWT is highly sensitive to the number of blades when Re_c is variable. For the two-bladed VAWT, the value of C_P decreases monotonically with the increase of σ, while the curve of C_P for the three-bladed VAWT shows a clear peak at $\sigma = 0.24$. Also, the two-bladed VAWT has a higher C_P when σ is relatively low, e.g., the value of C_P for $n = 2$ is 4.17% higher than that for $n = 3$ when $\sigma = 0.12$. In contrast, the three-bladed VAWT performs better when $\sigma = 0.36$. For a moderate σ of 0.24, the two- and three-bladed VAWTs have nearly the same power performance. Overall, for a given relatively low rotor solidity, the two-bladed design is expected to achieve higher peak power performance, while the three-bladed design is more advantageous when the rotor solidity is relatively high.

Fig. 15 shows the instantaneous lift coefficients and drag coefficients of the blades during one turbine revolution for different numbers of blades. For the curves of C_L, the increase of n is found to decrease the values of C_L in the upwind region and accelerate its decrease. This is because a shorter chord length will lead to a lower reduced frequency (Rezaeiha et al., 2018a), which has been proven to decrease the maximum C_L and promote the dynamic stall (Rezaeiha et al., 2018b), (Lee and Gerontakos, 2004). In the downwind region, the increase of n leads to an increase in the absolute valley values of C_L. This phenomenon becomes more intense when σ increases from 0.12 to 0.36. For the curves of C_D, the values of C_D in the upwind region decrease significantly with the increase of n, e.g., the peak value of C_D for $n = 3$ is 19.14% lower than that for $n = 2$ when $\sigma = 0.36$. The decrease of C_D compensates the negative impact of the decreased C_L, which results in the increase of C_P shown in Fig. 14. Also, the increase of n is found to increase the values of C_D in the downwind region. This may be due to the strong blade-wake interactions induced by the vortices shedding from more blades.

Fig. 16 shows the instantaneous torque coefficients of the blades and their normalized cumulative sums during one turbine revolution for different numbers of blades. It can be seen that the increase of n significantly decreases the values of C_Q in the upwind region, while the C_Q is less sensitive to the variation of n in the downwind region due to the low flow velocity. Also, as noted in previous studies (Rezaeiha et al., 2018b), (Zhu et al., 2019), the higher n will reduce the fluctuations in rotor torque, resulting in a more uniform power output. This is further confirmed by Fig. 16(b), in which the higher n is found to reduce the relative power contribution in the upwind region, allowing the VAWT to absorb energy more gradually during its rotation, especially for the relatively low σ.

Fig. 17 illustrates the instantaneous dimensionless vorticity distributions at the mid-span section of the blades for different numbers of blades. It can be seen that the increase of n slightly promotes the flow separation on the suction side of the blades. This is because for a given σ, the three-bladed VAWT has a shorter chord length and therefore a lower reduced frequency, which will lead to a lower separation resistance within the blade boundary layer (Rezaeiha et al., 2018b), (Lee and Gerontakos, 2004). Also, the lower Re_c experienced by the three-bladed

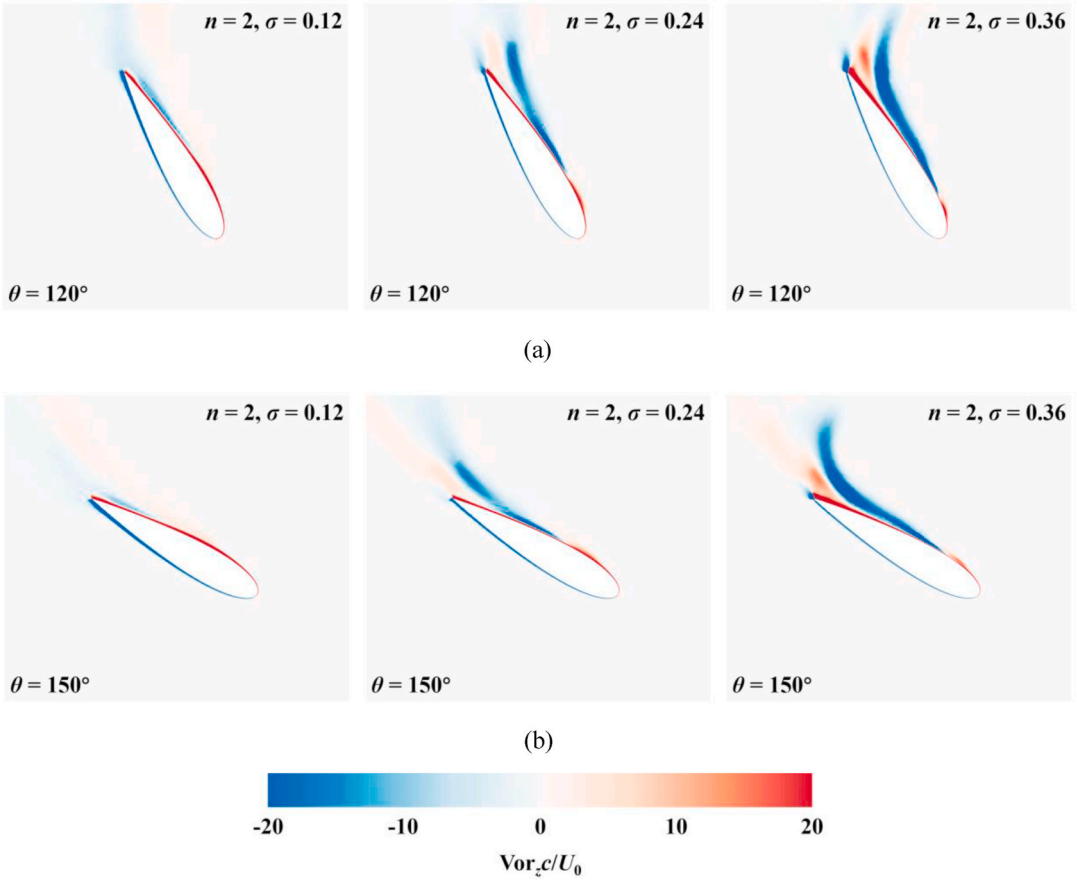

Fig. 12. Instantaneous dimensionless vorticity distributions at the tip section of the blades for different rotor solidities: (a) $\theta = 120°$; (b) $\theta = 150°$. (Modifying chord length, $n = 2$, $D = 1$ m).

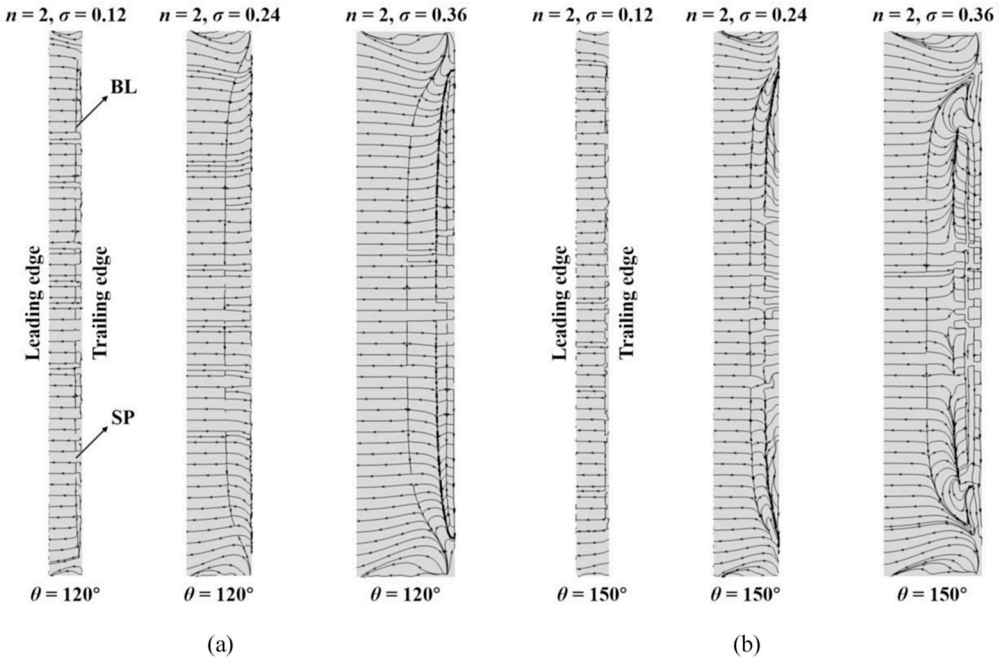

Fig. 13. Instantaneous streamline distributions on the suction side of the blades for different rotor solidities: (a) $\theta = 120°$; (b) $\theta = 150°$. (BL: bifurcation line, SP: saddle point, modifying chord length, $n = 2$, $D = 1$ m).

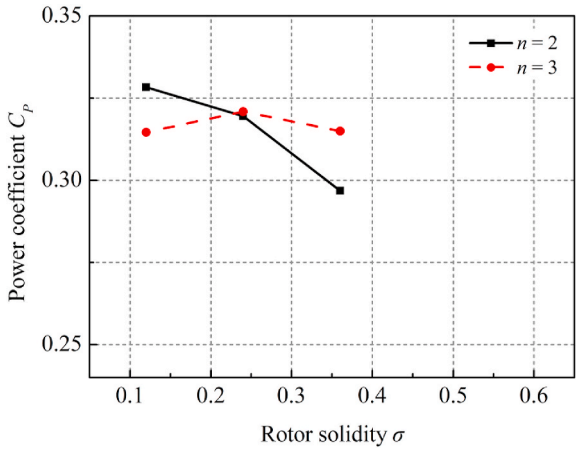

Fig. 14. Average power coefficients of VAWTs with different numbers of blades. ($D = 1$ m).

VAWT contributes to the early onset of flow separation. These undesired characteristics lead to the lower C_P of the three-bladed VAWT for $\sigma = 0.12$, as shown in Fig. 14. Nevertheless, the increase of n will result in a larger blade aspect ratio, which is expected to diminish the tip loss effect and improve the blade aerodynamics (Zanforlin and Deluca, 2018), (Hand and Cashman, 2017), especially for high-solidity VAWTs. As can be seen in Fig. 18, when $\sigma = 0.36$, the strength of the tip vortices for the three-bladed VAWT is significantly lower than that for the two-bladed one. Meanwhile, the larger blade aspect ratio restricts the development of spanwise flow (refer to Fig. 19), which will reduce the complexity of the flow patterns and increase the blade torque, corresponding to the higher C_P of the three-bladed VAWT for $\sigma = 0.36$.

4.3. Effect of rotor diameter

Fig. 20 shows the average power coefficients of two-bladed VAWTs with different rotor diameters. The σ and TSR_{opt} of the VAWT are fixed at 0.24 and 2.702, respectively (refer to Table 1(a) and Fig. 2(c)). It can be seen that when D is smaller than 1.25 m, its impact on the peak power performance of the VAWT is negligible, in which the value of C_P varies in a small range of 0.3184–0.3205, and a slight increase is observed when D increases from 0.75 m to 1.25 m. In contrast, the C_P is found to be more sensitive to the variation of D when D is relatively large. As D increases from 1.25 m to 2 m, the value of C_P decreases monotonically from 0.3205 to 0.3017. On the one hand, the chord length increases with the increase of the rotor diameter, allowing the blades to experience higher Reynolds numbers, which is expected to improve the turbine performance (Li et al., 2022), (Roh and Kang, 2013). However, since the inflow velocity is fixed for the test cases, the Reynolds number effect is not as pronounced as that in the study of Rezaeiha et al. (2018a), in which the Reynolds number is changed via the inflow velocity. On the other hand, the blade aspect ratio decreases with the increase of the rotor diameter, which will intensify the tip loss effect and deteriorate the turbine performance (Peng et al., 2022), (Miao et al., 2022). As noted in the study of Zanforlin and Deluca, 2018, when the turbine size is relatively small, the positive impact of the increased Reynolds number and the negative impact of the decreased blade aspect ratio will be delicately balanced, corresponding to the negligible variation of C_P for rotor diameters smaller than 1.25 m. As the rotor diameter increases further, the tip loss effect suppresses the Reynolds number effect, which leads to the decrease of C_P. These phenomena reflect the complexity of scale effect and imply that global optimal design is necessary for improving the turbine performance. Overall, for urban scales, the effect of rotor diameter is not significant at a fixed inflow velocity, and VAWTs with smaller rotor diameters perform relatively better.

Fig. 21 shows the instantaneous lift coefficients and drag coefficients of the blades during one turbine revolution for different rotor diameters. It can be seen that at the beginning of the revolution ($0° \leq \theta \leq 30°$), the larger D results in higher C_L and C_D. In the remaining upwind region, the values of C_L and C_D decrease continuously as D increases from 0.5 m to 2 m. For example, the peak values of C_L and C_D for $D = 2$ m are 17.57% and 11.33% lower than those for $D = 0.5$ m, respectively. The decrease of C_L is mainly due to the tip loss effect induced by the decreased blade aspect ratio, in which the tip vortices will reduce the local pressure difference between the suction and pressure sides of the blades, known as the flow leakage phenomenon (Zanforlin and Deluca, 2018). The spanwise propagation of tip vortices will also deteriorate the blade aerodynamics. For the decrease of C_D, the Reynolds number effect contributes the most, as the increased Reynolds number can reduce the turbulent shear stress on the blades, promote the transition from laminar to turbulent flows, delay the flow separation, and consequently improve the blade aerodynamics (Rezaeiha et al., 2018a). In the region of $180° \leq \theta \leq 300°$, the increase of D is found to increase the absolute values of C_L and decrease the C_D. Also, more fluctuations are observed in the curves of C_L and C_D, which may be due to the stronger blade-wake interactions.

Fig. 22 shows the instantaneous torque coefficients of the blades and their normalized cumulative sums during one turbine revolution for

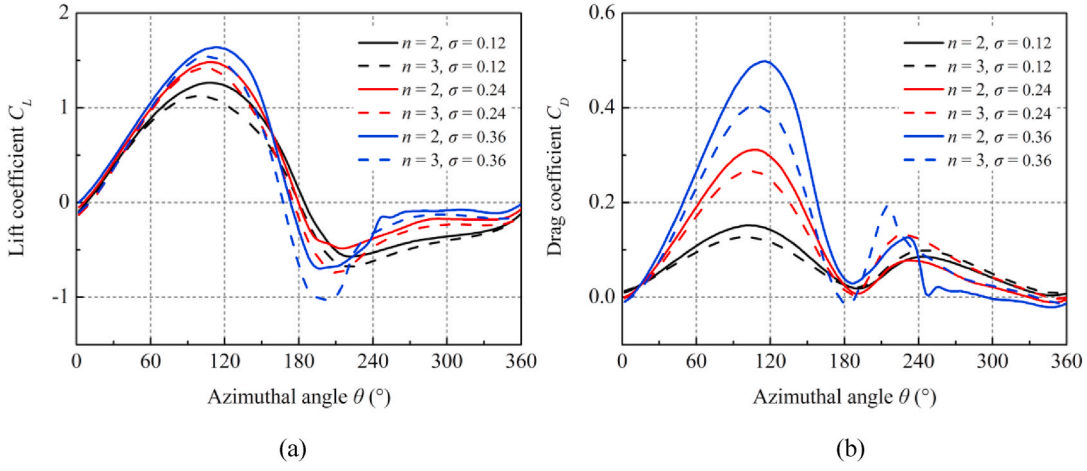

Fig. 15. Instantaneous lift coefficients and drag coefficients of the blades during one turbine revolution for different numbers of blades: (a) lift coefficient; (b) drag coefficient. ($D = 1$ m).

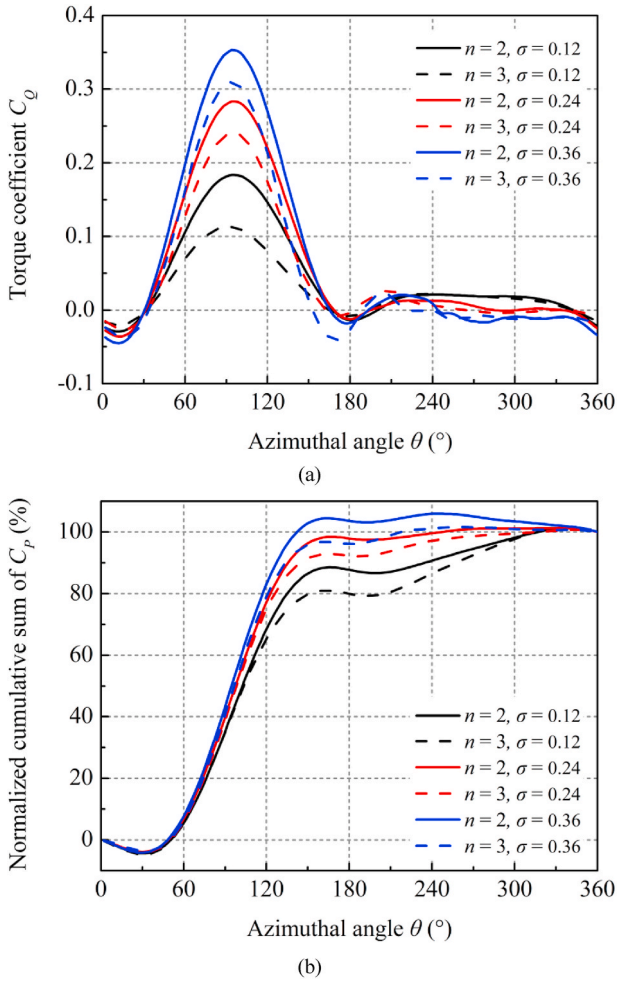

Fig. 16. Instantaneous torque coefficients of the blades and their normalized cumulative sums during one turbine revolution for different numbers of blades: (a) torque coefficient; (b) normalized cumulative sum. ($D = 1$ m).

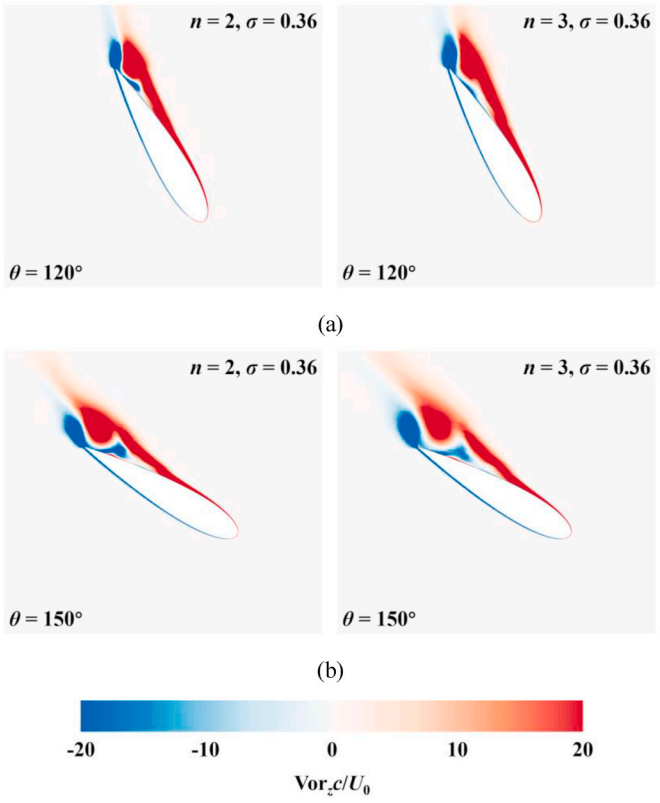

Fig. 17. Instantaneous dimensionless vorticity distributions at the mid-span section of the blades for different numbers of blades: (a) $\theta = 120°$; (b) $\theta = 150°$. ($D = 1$ m, $\sigma = 0.36$).

different rotor diameters. As expected, VAWTs with larger D have higher C_Q in the region of $0° \leq \theta \leq 60°$, which corresponds to the higher C_L shown in Fig. 21. In the remaining upwind region, the values of C_Q decrease monotonically with the increase of D, e.g., the peak value of C_Q for $D = 2$ m is 4.60% lower than that for $D = 0.5$ m, which leads to the lower C_P shown in Fig. 20. In the downwind region, higher C_Q is observed for larger D due to the increase of C_L and decrease of C_D. As shown in Fig. 22(b), the relative power contribution in the upwind region decreases with the increase of D, while the energy left for absorption in the downwind region increases. Therefore, VAWTs with larger rotor diameters have more uniform power output.

In addition, to investigate the significance of different geometrical parameters and the interactions between them, a parametric study based on response surface methodology (Box and Wilson, 1951) is conducted. The details are provided in Supplementary material S.3.

5. Effect of rotor solidity at fixed chord-based Reynolds numbers

In this section, the effect of rotor solidity on the power performance and aerodynamics of VAWTs at fixed chord-based Reynolds numbers is investigated. As listed in Table 1(b), the number of blades and rotor diameter are modified to change the turbine geometry, and the inflow velocity is modified correspondingly to keep the chord-based Reynolds number invariant. The turbine performance as well as the dynamic loads and flow patterns on the blades are systematically analyzed.

5.1. Effect of number of blades

Fig. 23 shows the average power coefficients of VAWTs with different numbers of blades at fixed chord-based Reynolds numbers. The two- and three-bladed VAWTs have the same σ, TSR_{opt}, and Re_c (refer to Table 1(b)). Note that the inflow velocity is modified to 13.95 m/s for all three-bladed VAWT cases to reach the Re_c for the two-bladed VAWT cases (Re_c fixed). The results of the three-bladed VAWT cases at variable Re_c are also included for comparison. It can be seen that at a given Re_c, the increase of n significantly improves the peak power performance of VAWTs with different σ, e.g., for $\sigma = 0.24$, the C_P of the three-bladed VAWT is 4.52% higher than that of the two-bladed one. Also, the fixed Re_c is found to affect the curves of C_P in two aspects. On the one hand, when Re_c is variable, the curve of C_P for $n = 3$ shows a clear peak at $\sigma = 0.24$, while when Re_c is fixed (increased), a similar trend to the curve of C_P for $n = 2$ is observed, in which the value of C_P decreases monotonically as σ increases from 0.12 to 0.36. This phenomenon confirms the hypothesis presented in Section 4.1 that different Reynolds

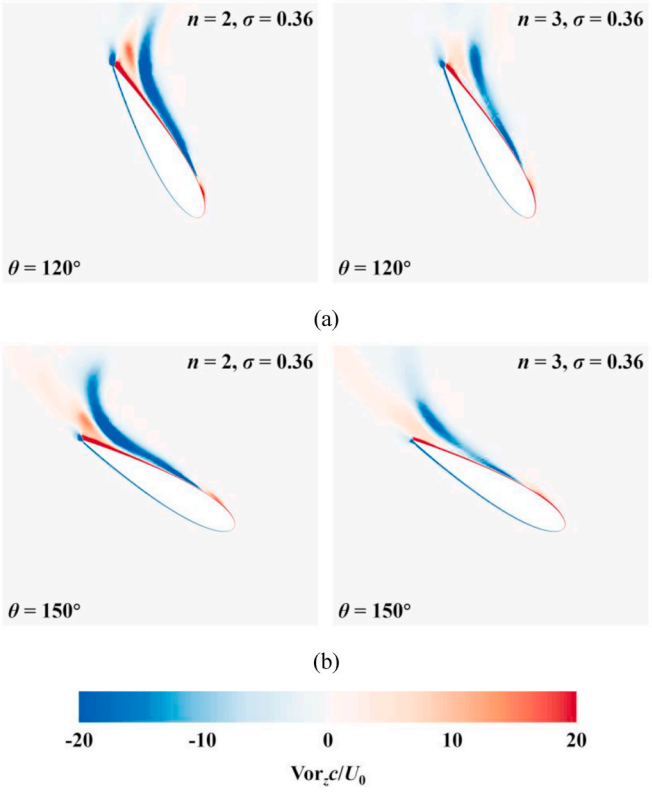

Fig. 18. Instantaneous dimensionless vorticity distributions at the tip section of the blades for different numbers of blades: (a) $\theta = 120°$; (b) $\theta = 150°$. ($D = 1$ m, $\sigma = 0.36$).

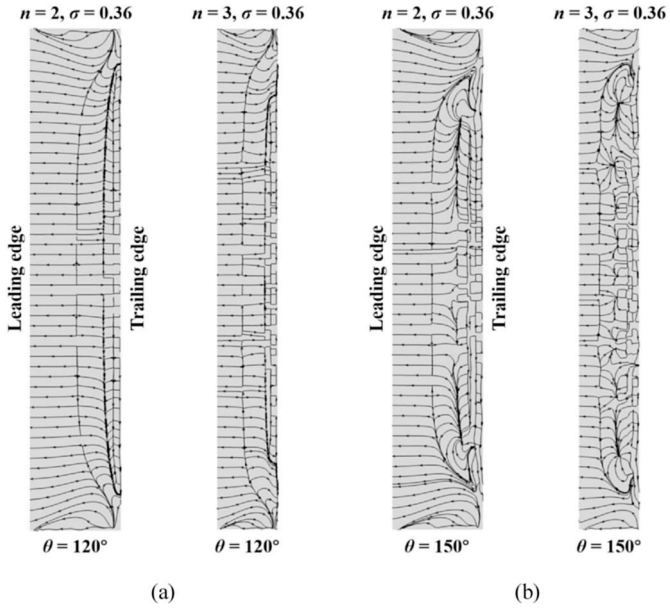

Fig. 19. Instantaneous streamline distributions on the suction side of the blades for different numbers of blades: (a) $\theta = 120°$; (b) $\theta = 150°$. ($D = 1$ m, $\sigma = 0.36$).

numbers induce the difference in the curves of C_P for two- and three-bladed VAWTs. On the other hand, due to the positive impact of the increased Reynolds number, the values of C_P for $n = 3$ increase significantly when Re_c is fixed, which is in agreement with the findings of

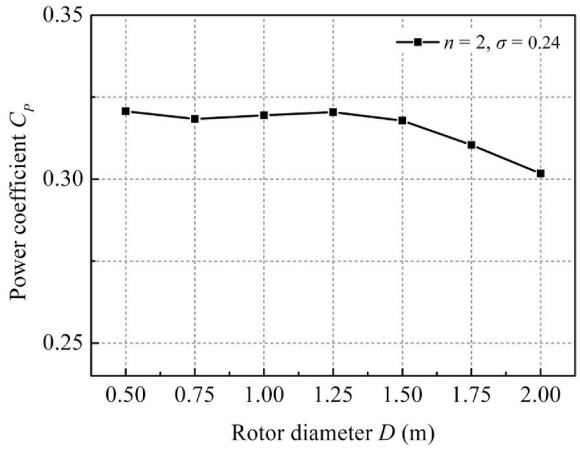

Fig. 20. Average power coefficients of two-bladed VAWTs with different rotor diameters. ($\sigma = 0.24$).

Rezaeiha et al. (2018a) and Bachant and Wosnik, 2016. Overall, when the chord-based Reynolds number is fixed, VAWTs with more blades can achieve higher peak power performance, and the variation of the number of blades will not affect the trend of the power coefficient versus rotor solidity curve.

Fig. 24 shows the instantaneous lift coefficients and drag coefficients of the blades during one turbine revolution for different numbers of blades at fixed chord-based Reynolds numbers. For the curves of C_L, it can be seen that when Re_c is fixed (increased), the values of C_L for $n = 3$ increase in the region of $60° \leq \theta \leq 150°$. In the downwind region, the C_L is found to be less sensitive to the variation of Re_c when σ is relatively low, e.g., for $\sigma = 0.12$, the values of C_L for $n = 3$ are nearly the same at variable and fixed Re_c. However, for higher σ, the Re_c has a significant impact on C_L in the region of $180° \leq \theta \leq 210°$, in which the absolute values of C_L for $n = 3$ decrease at fixed Re_c. For the curves of C_D, the fixed Re_c somewhat surprisingly leads to higher C_D in the upwind region when $\sigma = 0.36$. This may be due to the complexity of the dynamic stall associated with higher σ, which is also reported in the study of Rezaeiha et al. (2018b). In addition, the fixed Re_c is found to reduce the fluctuations of C_D in the downwind region.

Fig. 25 illustrates the instantaneous dimensionless vorticity distributions at the mid-span section of the blades at variable and fixed chord-based Reynolds numbers. It can be seen that when Re_c is fixed (increased), the flow separation on the suction side of the blades is slightly delayed, the roll-up vortices near the trailing edge are diminished, and the strength of the vortices shedding from the blunt trailing edge is reduced. Also, the fixed Re_c has a negligible impact on the tip loss effect, in which the vorticity field around the blade tips remains nearly unchanged (refer to Fig. 26). Further observation of the streamline distributions illustrated in Fig. 27 reveals that the bifurcation line moves toward the trailing edge, indicating that the fixed Re_c resists the flow separation on the blades. In addition, the flow patterns near the trailing edge become more stable, in which the spanwise flow induced by the roll-up vortices is suppressed. These changes significantly improve the turbine performance, resulting in the higher C_P shown in Fig. 23.

5.2. Effect of rotor diameter

Fig. 28 shows the average power coefficients of two-bladed VAWTs with different rotor diameters at fixed chord-based Reynolds numbers. The σ, TSR_{opt}, and Re_c are fixed at 0.24, 2.702, and 2.64×10^5, respectively (refer to Table 1(b)). Note that the inflow velocity for each case is modified to reach the Re_c for the case of $D = 1$ m. It can be seen that at a given Re_c, the increase of D deteriorates the peak power performance of VAWTs with the same σ, e.g., the value of C_P for $D = 2$ m is

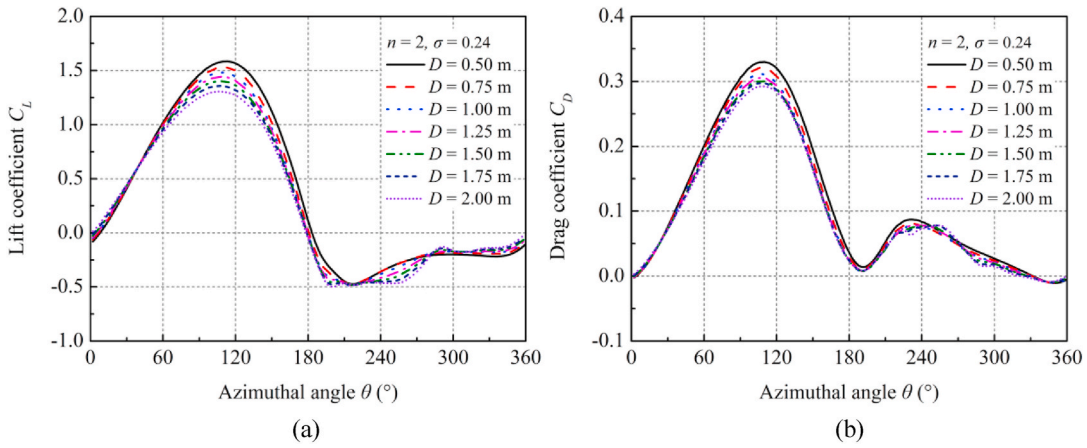

Fig. 21. Instantaneous lift coefficients and drag coefficients of the blades during one turbine revolution for different rotor diameters: (a) lift coefficient; (b) drag coefficient. ($n = 2$, $\sigma = 0.24$).

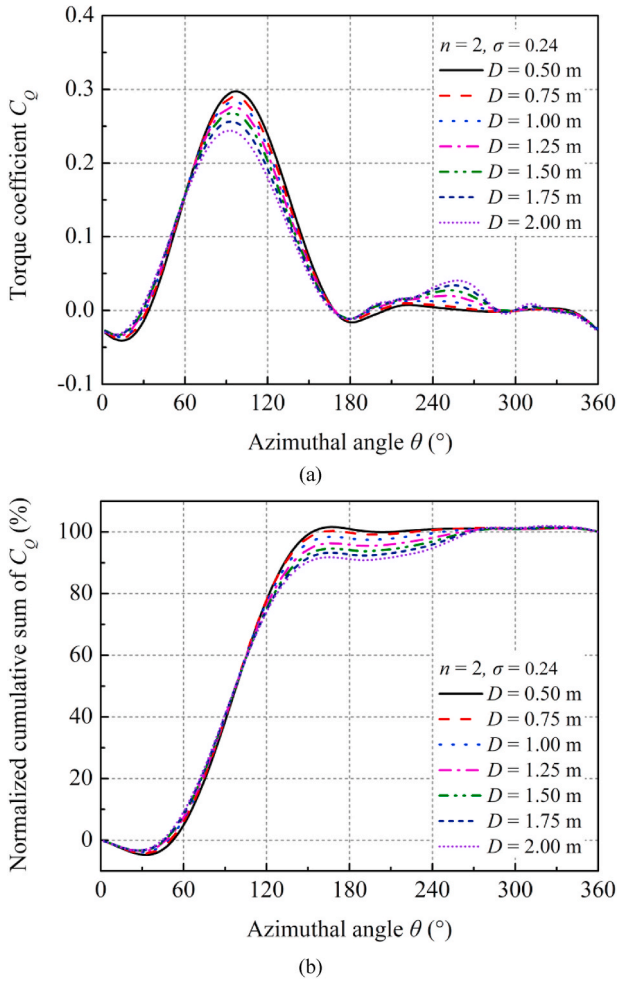

Fig. 22. Instantaneous torque coefficients of the blades and their normalized cumulative sums during one turbine revolution for different rotor diameters: (a) torque coefficient; (b) normalized cumulative sum. ($n = 2$, $\sigma = 0.24$).

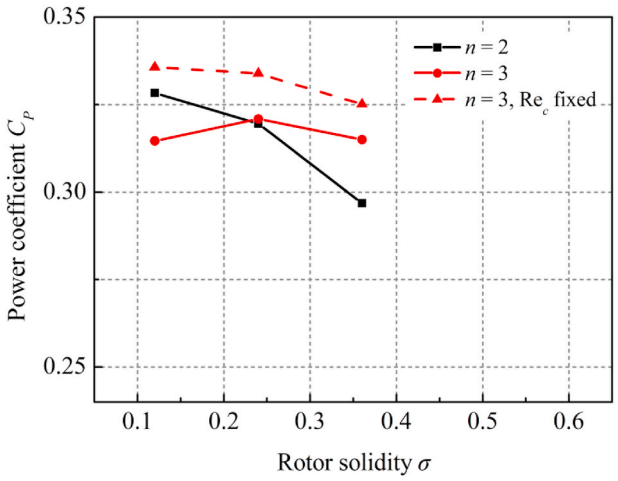

Fig. 23. Average power coefficients of VAWTs with different numbers of blades at fixed chord-based Reynolds numbers. ($D = 1$ m, fixed $\mathrm{Re}_c = 1.71 \times 10^5$, 2.64×10^5, and 3.38×10^5 for $\sigma = 0.12$, 0.24, and 0.36, respectively).

21.93% lower than that for $D = 0.5$ m. Also, the fixed Re_c is found to increase the sensitive of C_P to the variation of D, especially when D is relatively small. This is because when Re_c is variable, as described in Section 4.3, the effect of rotor diameter is a combination of Reynolds number effect and tip loss effect, while when Re_c is fixed, the Reynolds number effect is avoided and the tip loss effect becomes dominant, thus negatively affecting the turbine performance as the blade aspect ratio decreases. Overall, the effect of rotor diameter is strongly affected by the variation of the chord-based Reynolds number, and VAWTs with small rotor diameters have appreciable peak power performance.

Fig. 29 shows the instantaneous lift coefficients and drag coefficients of the blades during one turbine revolution for different rotor diameters at fixed chord-based Reynolds numbers. For the curves of C_L, it can be seen that when Re_c is fixed, the values of C_L for $D = 0.5$ m increase in the region of $60° \leq \theta \leq 180°$, while those for $D = 1.25$ m and 2 m decrease. This is because when $D = 0.5$ m, the inflow velocity experienced by the VAWT is modified from 9.3 m/s to 18.6 m/s to keep the Re_c fixed at 2.64×10^5, and the increased Reynolds number improves the blade aerodynamics. While for the cases of $D = 1.25$ m and 2 m, the inflow velocity is modified to 7.44 m/s and 4.65 m/s, respectively, and the blade aerodynamics deteriorates correspondingly. In the early downwind region, due to the deteriorated turbine performance and less energy absorption in the upwind region for larger D at fixed Re_c, the absolute values of C_L increase as D increases from 0.5 m to 2 m. For the curves of

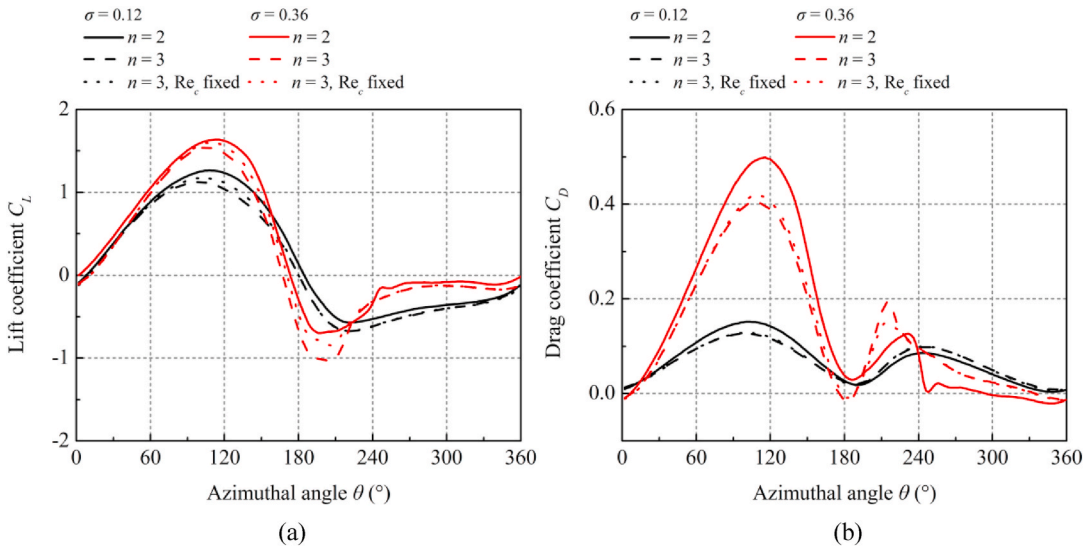

Fig. 24. Instantaneous lift coefficients and drag coefficients of the blades during one turbine revolution for different numbers of blades at fixed chord-based Reynolds numbers: (a) lift coefficient; (b) drag coefficient. (D = 1 m, fixed Re_c = 1.71 × 10^5, 2.64 × 10^5, and 3.38 × 10^5 for σ = 0.12, 0.24, and 0.36, respectively).

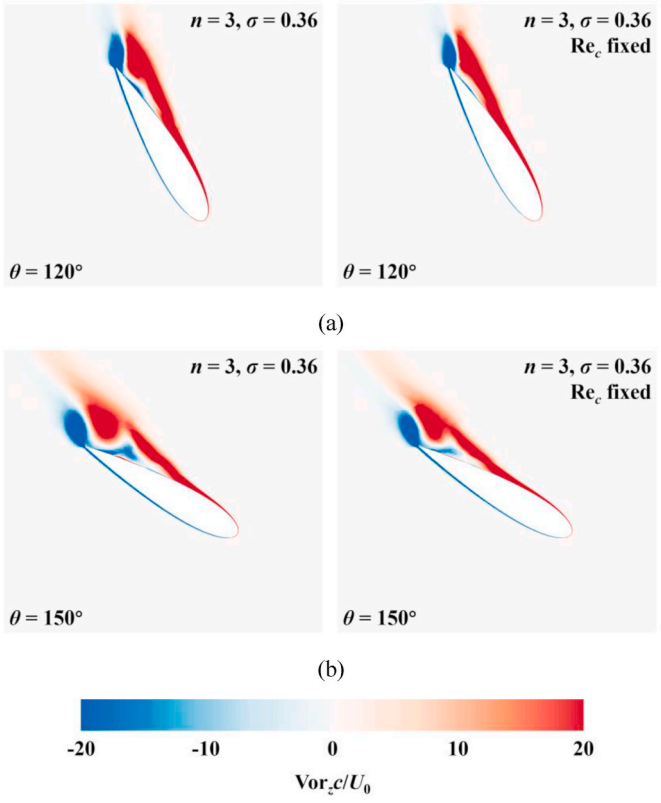

Fig. 25. Instantaneous dimensionless vorticity distributions at the mid-span section of the blades at variable and fixed chord-based Reynolds numbers: (a) θ = 120°; (b) θ = 150°. (n = 3, D = 1 m, σ = 0.36, fixed Re_c = 3.38 × 10^5).

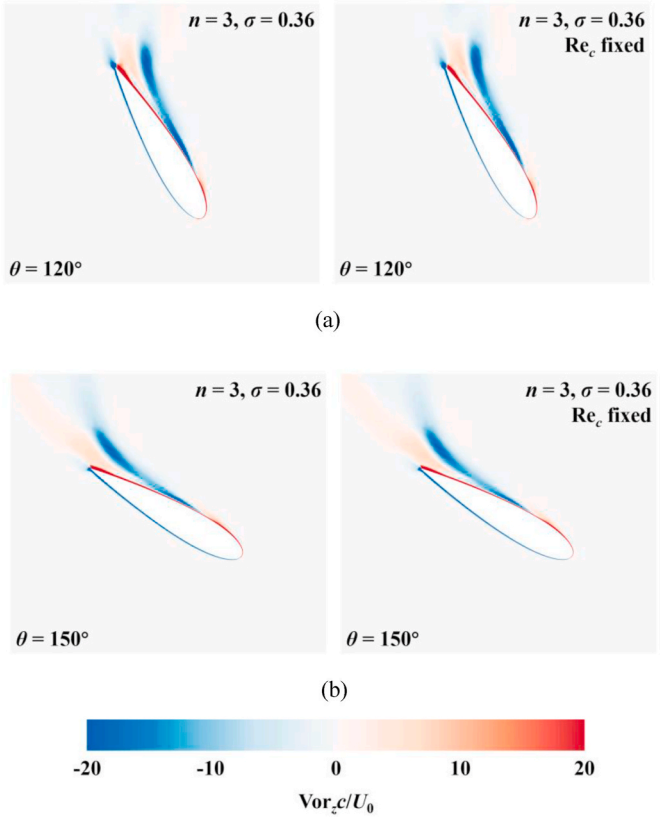

Fig. 26. Instantaneous dimensionless vorticity distributions at the tip section of the blades at variable and fixed chord-based Reynolds numbers: (a) θ = 120°; (b) θ = 150°. (n = 3, D = 1 m, σ = 0.36, fixed Re_c = 3.38 × 10^5).

C_D, the fixed (increased) Re_c is found to slightly increase the values of C_D in the region of 90° ≤ θ ≤ 180° for D = 0.5 m. This unexpected phenomenon can be interpreted by the complexity of the Reynolds number effect on the dynamic stall (Singleton and Yeager, 2000). Also, due to the negative impact of the decreased Reynolds number, a significant increase of C_D is observed in the region of 210° ≤ θ ≤ 240° for D = 2 m. Overall, when Re_c is fixed, the effect of rotor diameter on the blade aerodynamics is mainly determined by the tip loss effect, which is similar to the effect of number of blades described in Section 5.1.

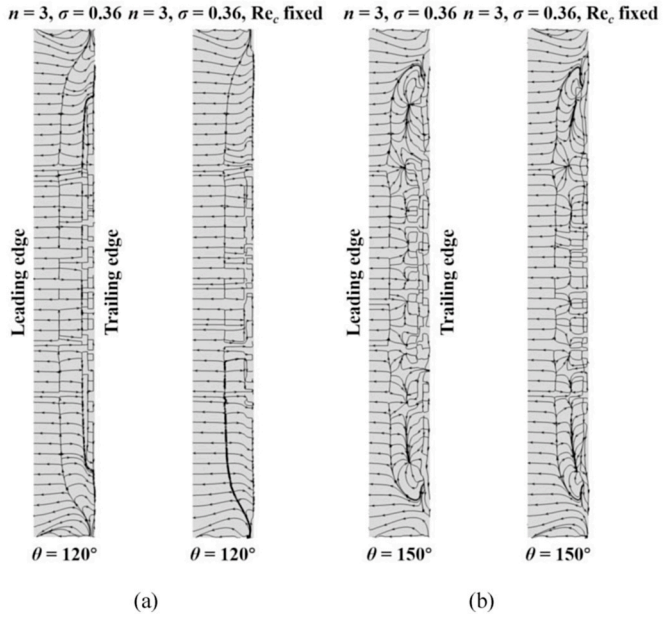

Fig. 27. Instantaneous streamline distributions on the suction side of the blades at variable and fixed chord-based Reynolds numbers: (a) $\theta = 120°$; (b) $\theta = 150°$. ($n = 3$, $D = 1$ m, $\sigma = 0.36$, fixed $Re_c = 3.38 \times 10^5$).

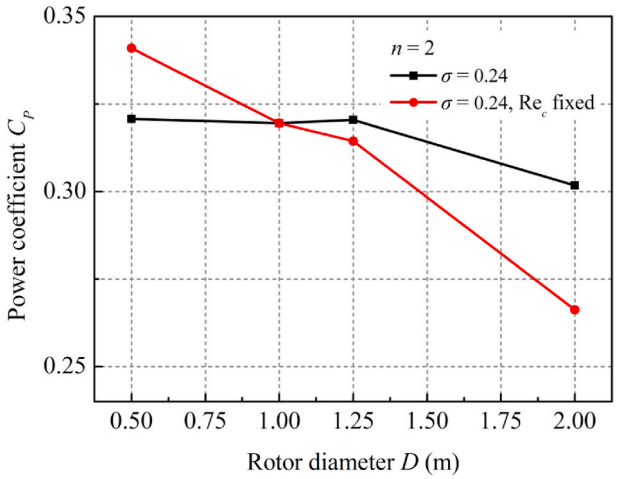

Fig. 28. Average power coefficients of two-bladed VAWTs with different rotor diameters at fixed chord-based Reynolds numbers. ($\sigma = 0.24$, fixed $Re_c = 2.64 \times 10^5$).

6. Conclusions

In the present study, high-fidelity improved delayed detached-eddy simulations are performed to investigate the effect of rotor solidity on the power performance and aerodynamics of VAWTs. Three key geometrical parameters, i.e., chord length, number of blades, and rotor diameter, are studied over a wide and reasonable range. The Reynolds number effect induced by the change of turbine geometry is considered, in which the solidity effects at variable and fixed chord-based Reynolds numbers are compared. The main findings are as follows.

- A low to moderate rotor solidity allows the VAWT to achieve appreciable peak power performance, while an excessively high rotor solidity (e.g., higher than 0.36) will reduce the peak turbine power. The large angle of attack experienced by the high-solidity VAWT promotes the flow separation and dynamic stall on the blades, the small blade aspect ratio intensifies the tip loss effect and complicates the spanwise flow structures, and the strong blade-wake interactions negatively affect the blade aerodynamics in the downwind region, thus deteriorating the turbine performance.
- When the inflow velocity is fixed, for a given relatively low rotor solidity (e.g., 0.12), the two-bladed design is expected to achieve higher peak turbine power because of the higher reduced frequency, while the three-bladed design is more advantageous when the rotor solidity is relatively high (e.g., 0.36), mainly due to the diminished tip loss effect. The Reynolds number effect leads to different trends in the power coefficient versus rotor solidity curves for VAWTs with different number of blades and the same rotor solidity.
- For urban scales, the effect of rotor diameter is not significant at a fixed inflow velocity and rotor solidity. When the rotor diameter is relatively small, the peak power performance of the VAWT varies in a small range due to the delicate balance of Reynolds number effect and tip loss effect. When the rotor diameter is larger than 1.25 m, the tip loss effect prevails and the turbine performance deteriorates as the rotor diameter increases further. Nevertheless, VAWTs with larger rotor diameters have more uniform power output.
- When the chord-based Reynolds number is fixed, for a given rotor solidity, VAWTs with more blades can achieve higher peak power performance due to the diminished tip loss effect, and the variation of the number of blades will not affect the trend of the power coefficient versus rotor solidity curve. The increased Reynolds number can resist the flow separation on the blades and suppress the spanwise flow.
- The effect of rotor diameter is strongly affected by the variation of the chord-based Reynolds number. The fixed chord-based Reynolds number increases the sensitivity of the turbine performance to the variation of the rotor diameter. For a given rotor solidity and chord-based Reynolds number, VAWTs with small rotor diameters have appreciable peak power performance.

CRediT authorship contribution statement

Limin Kuang: Conceptualization, Methodology, Software, Validation, Formal analysis, Writing – original draft. **Rui Zhang:** Software, Formal analysis, Writing – original draft. **Jie Su:** Methodology, Writing – review & editing. **Yixiao Shao:** Writing – review & editing. **Kai Zhang:** Writing – review & editing, Supervision. **Yaoran Chen:** Writing – review & editing. **Zhihao Zhang:** Formal analysis. **Yu Tu:** Formal analysis. **Dai Zhou:** Resources, Writing – review & editing, Supervision, Funding acquisition. **Zhaolong Han:** Resources, Supervision, Funding acquisition. **Yan Bao:** Supervision. **Yong Cao:** Supervision.

Declaration of competing interest

The authors declare that they have no known competing financial interests or personal relationships that could have appeared to influence the work reported in this paper.

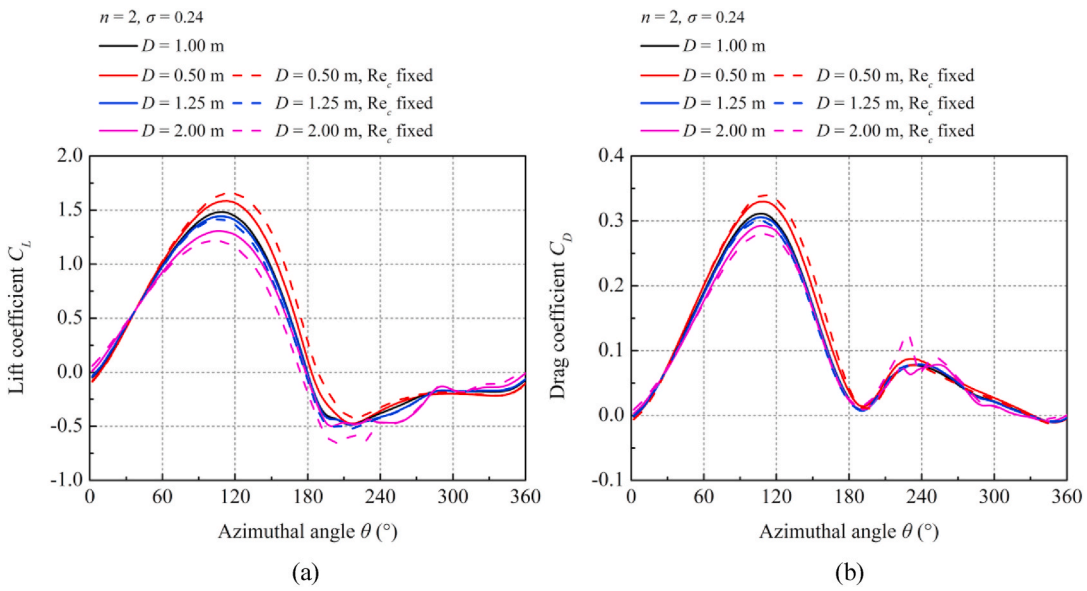

Fig. 29. Instantaneous lift coefficients and drag coefficients of the blades during one turbine revolution for different rotor diameters at fixed chord-based Reynolds numbers: (a) lift coefficient; (b) drag coefficient. ($n = 2$, $\sigma = 0.24$, fixed $Re_c = 2.64 \times 10^5$).

Data availability

Data will be made available on request.

Acknowledgments

The financial supports from the Innovation Program of Shanghai Municipal Education Commission (No. 2019-01-07-00-02-E00066), National Natural Science Foundation of China (Nos. 52122110 and 42076210), Shuguang Program of Shanghai Education Development Foundation and Shanghai Municipal Education Commission (No. 19SG10), Oceanic Interdisciplinary Program of Shanghai Jiao Tong University (No. SL2020PT201), and China Scholarship Council (No. 202206230089) are gratefully acknowledged. Limin Kuang and Rui Zhang contributed equally to this study.

Appendix A. Supplementary data

Supplementary data to this article can be found online at https://doi.org/10.1016/j.jweia.2022.105284.

References

Al-Shetwi, A.Q., 2022. Sustainable development of renewable energy integrated power sector: trends, environmental impacts, and recent challenges. Sci. Total Environ. 822, 153645.
Bachant, P., Wosnik, M., 2016. Effects of Reynolds number on the energy conversion and near-wake dynamics of a high solidity vertical-axis cross-flow turbine. Energies 9 (2), 73.
Balduzzi, F., Bianchini, A., Maleci, R., Ferrara, G., Ferrari, L., 2016. Critical issues in the CFD simulation of Darrieus wind turbines. Renew. Energy 85, 419–435.
Bhargav, M.M.S.R.S., Ratna Kishore, V., Laxman, V., 2016. Influence of fluctuating wind conditions on vertical axis wind turbine using a three dimensional CFD model. J. Wind Eng. Ind. Aerod. 158, 98–108.
Box, G.E.P., Wilson, K.B., 1951. On the experimental attainment of optimum conditions. J R Stat Soc Ser B-Stat Methodol 13 (1), 1–45.
CD-adapco, 2018. STAR-CCM+ User Guide Version 13.04. CD-adapco, New York, NY, USA.
Celik, Y., Ma, L., Ingham, D., Pourkashanian, M., 2020. Aerodynamic investigation of the start-up process of H-type vertical axis wind turbines using CFD. J. Wind Eng. Ind. Aerod. 204, 104252.
Chen, L., Yang, Y., Gao, Y., Gao, Z., Guo, Y., Sun, L., 2019. A novel real-time feedback pitch angle control system for vertical-axis wind turbines. J. Wind Eng. Ind. Aerod. 195, 104023.
Claessens, M.C., 2006. The Design and Testing of Airfoils for Application in Small Vertical axis Wind Turbines. Delft University of Technology, Delft.
Dilimulati, A., Stathopoulos, T., Paraschivoiu, M., 2018. Wind turbine designs for urban applications: a case study of shrouded diffuser casing for turbines. J. Wind Eng. Ind. Aerod. 175, 179–192.
Eboibi, O., Danao, L.A.M., Howell, R.J., 2016. Experimental investigation of the influence of solidity on the performance and flow field aerodynamics of vertical axis wind turbines at low Reynolds numbers. Renew. Energy 92, 474–483.
Edwards, J.M., 2012. The Influence of Aerodynamic Stall on the Performance of Vertical axis Wind Turbines. University of Sheffield, Sheffield.
Elkhoury, M., Kiwata, T., Aoun, E., 2015. Experimental and numerical investigation of a three-dimensional vertical-axis wind turbine with variable-pitch. J. Wind Eng. Ind. Aerod. 139, 111–123.
Ferreira, C.S., Geurts, B., 2015. Aerofoil optimization for vertical-axis wind turbines. Wind Energy 18 (8), 1371–1385.
Gosselin, R., Dumas, G., Boudreau, M., 2016. Parametric study of H-Darrieus vertical-axis turbines using CFD simulations. J. Renew. Sustain. Energy 8 (5), 053301.
Hand, B., Cashman, A., 2017. Conceptual design of a large-scale floating offshore vertical axis wind turbine. Energy Proc. 142, 83–88.
Hand, B., Kelly, G., Cashman, A., 2021. Aerodynamic design and performance parameters of a lift-type vertical axis wind turbine: a comprehensive review. Renew. Sustain. Energy Rev. 139, 110699.
Hassan, S.M.R., Ali, M., Islam, M.Q., 2016. The effect of solidity on the performance of H-rotor Darrieus turbine. AIP Conf. Proc. 1754, 040012.
Kuang, L., Lei, H., Zhou, D., Han, Z., Bao, Y., Zhao, Y., 2021. Numerical investigation of effects of turbulence intensity on aerodynamic performance for straight-bladed vertical-axis wind turbines. J Energy Eng-ASCE 147 (1), 04020087.
Kuang, L., Su, J., Chen, Y., Han, Z., Zhou, D., Zhang, K., et al., 2022a. Wind-capture-accelerate device for performance improvement of vertical-axis wind turbines: external diffuser system. Energy 239, 122196.
Kuang, L., Lu, Q., Huang, X., Song, L., Chen, Y., Su, J., et al., 2022b. Characterization of wake interference between two tandem offshore floating vertical-axis wind turbines: effect of platform pitch motion. Energy Convers. Manag. 265, 115769.
Lam, H., Liu, Y., Peng, H., Lee, C., Liu, H., 2018. Assessment of solidity effect on the power performance of H-rotor vertical axis wind turbines in turbulent flows. J. Renew. Sustain. Energy 10 (2), 023304.
Lee, T., Gerontakos, P., 2004. Investigation of flow over an oscillating airfoil. J. Fluid Mech. 512, 313–341.
Lei, H., Zhou, D., Bao, Y., Li, Y., Han, Z., 2017. Three-dimensional improved delayed detached eddy simulation of a two-bladed vertical axis wind turbine. Energy Convers. Manag. 133, 235–248.
Li, Q., Maeda, T., Kamada, Y., Murata, J., Shimizu, K., Ogasawara, T., et al., 2016. Effect of solidity on aerodynamic forces around straight-bladed vertical axis wind turbine by wind tunnel experiments (depending on number of blades). Renew. Energy 96, 928–939.
Li, Q., Maeda, T., Kamada, Y., Shimizu, K., Ogasawara, T., Nakai, A., et al., 2017. Effect of rotor aspect ratio and solidity on a straight-bladed vertical axis wind turbine in three-dimensional analysis by the panel method. Energy 121, 1–9.
Li, G., Xu, W., Li, Y., Wang, F., 2022. Univariate analysis of scaling effects on the aerodynamics of vertical axis wind turbines based on high-resolution numerical simulations: the Reynolds number effects. J. Wind Eng. Ind. Aerod. 223, 104938.

McIntosh, S.C., 2009. Wind Energy for the Built Environment. University of Cambridge, Cambridge.
Mendoza, V., Bachant, P., Ferreira, C., Goude, A., 2019. Near-wake flow simulation of a vertical axis turbine using an actuator line model. Wind Energy 22 (2), 171–188.
Miao, W., Liu, Q., Xu, Z., Yue, M., Li, C., Zhang, W., 2022. A comprehensive analysis of blade tip for vertical axis wind turbine: aerodynamics and the tip loss effect. Energy Convers. Manag. 153, 115140.
Molina, A.C., De Troyer, T., Massai, T., Vergaerde, A., Runacres, M.C., Bartoli, G., 2019. Effect of turbulence on the performance of VAWTs: an experimental study in two different wind tunnels. J. Wind Eng. Ind. Aerod. 193, 103969.
Peng, H., Lam, H., Liu, H., 2019. Power performance assessment of H-rotor vertical axis wind turbines with different aspect ratios in turbulent flows via experiments. Energy 173, 121–132.
Peng, H., Liu, M., Liu, H., Lin, K., 2022. Optimization of twin vertical axis wind turbines through large eddy simulations and Taguchi method. Energy 240, 122560.
Posa, A., 2020. Influence of tip speed ratio on wake features of a vertical Axis wind turbine. J. Wind Eng. Ind. Aerod. 197, 104076.
Posa, A., 2021. Secondary flows in the wake of a vertical axis wind turbine of solidity 0.5 working at a tip speed ratio of 2.2. J. Wind Eng. Ind. Aerod. 213, 104621.
Rezaeiha, A., 2019. Characterization and Improvement of Aerodynamic Performance of Vertical axis Wind Turbines Using Computational Fluid Dynamics. Technische Universiteit Eindhoven, Eindhoven.
Rezaeiha, A., Kalkman, I., Blocken, B., 2017a. Effect of pitch angle on power performance and aerodynamics of a vertical axis wind turbine. Appl. Energy 197, 132–150.
Rezaeiha, A., Kalkman, I., Montazeri, H., Blocken, B., 2017b. Effect of the shaft on the aerodynamic performance of urban vertical axis wind turbines. Energy Convers. Manag. 149, 616–630.
Rezaeiha, A., Kalkman, I., Blocken, B., 2017c. CFD simulation of a vertical axis wind turbine operating at a moderate tip speed ratio: guidelines for minimum domain size and azimuthal increment. Renew. Energy 107, 373–385.
Rezaeiha, A., Montazeri, H., Blocken, B., 2018a. Characterization of aerodynamic performance of vertical axis wind turbines: impact of operational parameters. Energy Convers. Manag. 169, 45–77.
Rezaeiha, A., Montazeri, H., Blocken, B., 2018b. Towards optimal aerodynamic design of vertical axis wind turbines: impact of solidity and number of blades. Energy 165, 1129–1148.
Rezaeiha, A., Montazeri, H., Blocken, B., 2019. Active flow control for power enhancement of vertical axis wind turbines: leading-edge slot suction. Energy 189, 116131.
Rogowski, K., Hansen, M.O.L., Bangga, G., 2020. Performance analysis of a H-Darrieus wind turbine for a series of 4-digit NACA airfoils. Energies 13 (12), 3196.
Roh, S., Kang, S., 2013. Effects of a blade profile, the Reynolds number, and the solidity on the performance of a straight bladed vertical axis wind turbine. J. Mech. Sci. Technol. 27 (11), 3299–3307.
Shur, M.L., Spalart, P.R., Strelets, M.K., Travin, A.K., 2008. A hybrid RANS-LES approach with delayed-DES and wall-modelled LES capabilities. Int. J. Heat Fluid Flow 29 (6), 1638–1649.
Singleton, J.D., Yeager Jr., W.T., 2000. Important scaling parameters for testing model-scale helicopter rotors. J. Aircraft 37 (3), 396–402.
Su, J., Chen, Y., Han, Z., Zhou, D., Bao, Y., Zhao, Y., 2020. Investigation of V-shaped blade for the performance improvement of vertical axis wind turbines. Appl. Energy 260, 114326.
Subramanian, A., Yogesh, S.A., Sivanandan, H., Giri, A., Vasudevan, M., Mugundhan, V., et al., 2017. Effect of airfoil and solidity on performance of small scale vertical axis wind turbine using three dimensional CFD model. Energy 133, 179–190.
Tescione, G., Ragni, D., He, C., Ferreira, C.J.S., van Bussel, G.J.W., 2014. Near wake flow analysis of a vertical axis wind turbine by stereoscopic particle image velocimetry. Renew. Energy 70, 47–61.
Tirandaz, M.R., Rezaeiha, A., 2021. Effect of airfoil shape on power performance of vertical axis wind turbines in dynamic stall: symmetric Airfoils. Renew. Energy 173, 422–441.
Yan, Y., Avital, E., Williams, J., Cui, J., 2021. Aerodynamic performance improvements of a vertical axis wind turbine by leading-edge protuberance. J. Wind Eng. Ind. Aerod. 211, 104535.
Zanforlin, S., Deluca, S., 2018. Effects of the Reynolds number and the tip losses on the optimal aspect ratio of straight-bladed Vertical Axis Wind Turbines. Energy 148, 179–195.
Zhang, T., Wang, Z., Huang, W., Ingham, G., Ma, L., Pourkashanian, M., 2020. A numerical study on choosing the best configuration of the blade for vertical axis wind turbines. J. Wind Eng. Ind. Aerod. 201, 104162.
Zhu, H., Hao, W., Li, C., Ding, Q., 2019. Numerical study of effect of solidity on vertical axis wind turbine with Gurney flap. J. Wind Eng. Ind. Aerod. 186, 17–31.